# The Physical Properties of Low-Redshift FeLoBAL Quasars: II. The Rest-Frame Optical Emission Line Properties

KAREN M. LEIGHLY, HYUNSEOP CHOI, CORA DEFRANCESCO, JULIANNA VOELKER, DONALD M. TERNDRUP, SARAH C. GALLAGHER, A, 5, 6 AND GORDON T. RICHARDS

<sup>1</sup>Homer L. Dodge Department of Physics and Astronomy, The University of Oklahoma, 440 W. Brooks St., Norman, OK 73019, USA

<sup>2</sup>Department of Astronomy, The Ohio State University, 140 W. 18th Ave., Columbus, OH 43210

<sup>3</sup>Department of Physics & Astronomy, The University of Western Ontario, London, ON, N6A 3K7, Canada

<sup>4</sup>Canadian Space Agency, 6767 Route de l'Aéroport, Saint-Hubert, Quebec, J3Y BY9

<sup>5</sup>Institute for Earth and Space Exploration, The University of Western Ontario, London, ON, N6A 3K7, Canada

<sup>6</sup>The Rotman Institute of Philosophy, The University of Western Ontario, London, ON, N6A 3K7, Canada

<sup>7</sup>Department of Physics, Drexel University, 32 S. 32nd St., Philadelphia, PA 19104

#### ABSTRACT

We report the results of analysis of the H $\beta$  emission-line region of a sample of thirty low-redshift (z < 1) iron low-ionization broad absorption line quasars (FeLoBALQs). Eleven of these objects are newly classified as FeLoBALQs. A matched sample of 132 unabsorbed quasars was analyzed in parallel. The emission lines showed the well known anticorrelation between the [O III] and Fe II emission (Boroson & Green 1992). Using a summary statistic called E1 to quantify this anticorrelation, we found that while the distribution of E1 for the unabsorbed quasars has a single peak, the FeLoBALQs have a bimodal shape in this parameter. Previous studies have shown that the line emission properties of BAL and non-BAL quasars are consistent, and therefore the difference in the H $\beta$  region emission between FeLoBAL quasars and unabsorbed quasars is a new result. The two populations of FeLoBAL quasars are characterized by low and high bolometric luminosities and Eddington ratios. Some previous studies have suggested that BAL quasars are high accretion-rate objects, and therefore the discovery of the low accretion-rate branch of FeLoBAL quasars was unexpected. We also found that the H $\beta$  FWHM is systematically broader among the FeLoBALQs compared with the non-BAL quasars implying a higher inclination viewing angle or a dearth of low-velocity line-emitting gas.

Keywords: Quasars; Broad-absorption line quasar

## 1. INTRODUCTION

Broad absorption lines occur in 10-26% of optically selected quasars (Tolea et al. 2002; Hewett & Foltz 2003; Reichard et al. 2003; Trump et al. 2006; Knigge et al. 2008; Gibson et al. 2009). The broad and blueshifted C IV absorption lines observed in broad absorption line quasars (BALQs) reveal an unambiguous signature of outflow. Therefore, BALQs may be important sources of quasar feedback in galaxy evolution. Trump et al. (2006) found that 1.3% of quasars have broad

at least some BAL quasars tends to be soft.

Mg II absorption; these are called low-ionization broad absorption line quasars (LoBALQs). A typical median width of a LoBALQ Mg II broad absorption line is 4400 km s<sup>-1</sup> (Yi et al. 2019). Trump et al. (2006) found that 0.3% of quasars also have absorption from Fe II, and these are called iron low-ionization broad absorption line quasars (FeLoBALQs). FeLoBAL quasars are rare, and previous to the Sloan Digital Sky Survey, only a few were known. For example, Hall et al. (2002) published spectra and discussed the wide range of features observed in 23 unusual objects discovered in the SDSS; many of those objects are FeLoBAL quasars.

How do BAL quasars, and FeLoBAL quasars specifically, fit in among quasars in general? Are they fundamentally the same, and their magnificent spectra are observed because of a select range of viewing angles? Or do they mark a special stage in quasar evolution? Or are both factors important? One way to address these questions is to look at the broad emission lines. Weymann et al. (1991) performed the first comprehensive study of the emission-line properties of BAL and unabsorbed quasars, focusing on the rest frame UV emission lines observed in ground-based spectra. They found that, with the exception of LoBAL quasars, the line emission was indistinguishable from that of unabsorbed quasars. This result makes sense if the emission lines in both type of objects originate in a similarly photoionized broad-line region (rather than, e.g., an expanding outflow like a supernova). Modern studies using larger samples have found a somewhat different pattern of behaviors that link the outflow properties with the emission line and continuum properties. For example, Baskin et al. (2015) reported that the He II $\lambda$ 1640 equivalent width is inversely related to the velocity shift and width of the BAL absorption. This result has been confirmed by further analysis (Hamann et al. 2019; Rankine et al. 2020). Because weak He II is a signature of a UV-dominant or soft spectral energy distribution (SED; e.g., Leighly 2004), these results may imply that the illuminating SED in

The rest-frame optical bandpass is arguably the best-studied region of quasar spectra, containing the  $H\beta$ , [O III], and Fe II lines that are routinely used to measure black hole masses and Eddington ratios. The rest-frame optical band has been less well studied in BAL quasars than the rest-frame UV band, because this band is observed in the near-infrared when C IV $\lambda$ 1549 is observed in the optical band. Yuan & Wills (2003) reported results from 16 BAL quasars and a comparison sample of 13 non-BAL quasars. They found that the [O III] lines are weak in BAL quasars. Runnoe et al. (2013) reported results from a sample of eight moderate-redshift radio-loud BALQs. They also found weak [O III] and strong Fe II in these objects suggesting a high accretion rate (e.g., Boroson 2002; Shen & Ho 2014). However, analysis of the Balmer-line widths and estimation of the black hole masses revealed the Eddington ratios that were consistent with comparable unabsorbed quasars. Schulze et al. (2017) presented the largest sample of LoBAL and FeLoBAL quasars studied in the rest-frame optical band, with near-IR spectroscopy from 16 LoBAL quasars and 6 FeLoBAL quasars. Sixteen of the spectra cover the  $H\beta/[O\ III]$  region. Their results deviate from the previous work: they saw neither notably weak [O III] nor notably strong Fe II emission. Instead, they found that their  $z \sim 1.5$  subsample composite spectrum may have weaker Fe II emission than the unabsorbed quasars.

These three studies of the rest-frame optical spectra of BAL quasars leave the impression that BAL quasars often appear to be high Eddington ratio objects. More recently, Rankine et al. (2020) estimated the Eddington ratio in BAL quasars using a reconstructed C IV emission line and a profile

correction (Coatman et al. 2017). They found that the Eddington ratio distribution is indistinguishable between broad absorption line quasars and unabsorbed quasars.

A complicating factor is the luminosity of the objects studied. Many quasar properties are luminosity dependent (e.g., the Baldwin effect; Baldwin 1977). BAL outflow velocities are observed to have a particularly strong dependence on quasar luminosity (e.g., Laor & Brandt 2002; Ganguly et al. 2007). This dependence may be expected; for a fixed  $L_{\rm Bol}/L_{\rm Edd}$ , a more luminous black hole will have a larger black hole mass. That larger black hole mass yields a spectral energy distribution (SED) that peaks at longer wavelengths. This softer SED may influence the outflows in two ways. 1.) Soft SEDs are less likely to over-ionize the outflowing gas. 2.) The soft SED produces a relatively higher flux density of the UV photons responsible for accelerating the outflow via resonance line driving. Quasar luminosity evolution and flux-limited surveys combine to yield higher-luminosity objects at larger redshifts (Jester et al. 2005). It is therefore not clear that samples of objects with different redshifts and luminosities can be compared directly.

This paper is the second in a series of four papers. Paper I (Choi et al. 2022) describes the SimBAL (Leighly et al. 2018) spectral synthesis analysis of the BAL outflows in fifty low redshift FeLoBAL quasars. In this paper, Paper II, we present analysis of the rest-frame optical band spectra of a subsample of thirty of the 50 FeLoBAL quasars considered in Choi et al. (2022). All of the objects in this subsample have redshifts z < 1 and the SDSS/BOSS spectra include the H $\beta$  / [O III] region of the spectrum. Paper III (Choi et al. submitted) combines the SimBAL results from Paper I and the emission-line analysis of this paper to discuss the implications for the location and geometry of the outflow. Paper IV (Leighly et al. in prep.) includes the broad-band optical/IR properties and discusses the potential implications for accretion models and evolution scenarios for low redshift FeLoBAL quasars.

Our paper is organized as follows. In  $\S1$ , we describe the data selection of the FeLoBAL quasars and a matched comparison sample of 132 unabsorbed quasars, the optical band modeling, and a principal components analysis of the spectrum around H $\beta$ . In  $\S3$ , we compare the optical and derived properties of the FeLoBAL quasars with those of the comparison sample. We present our reasoning and methodology for dividing the FeLoBAL quasars into two groups. We also look at correlations and patterns among the emission-line and global properties and compare with previous results from the literature.  $\S4$  summarizes our results.

#### 2. DATA

## 2.1. Sample Selection

The parent sample of the FeLoBALQs was drawn from the literature, from the sample of 0.8 < z < 3.0 FeLoBALQ candidates found in the DR14 quasar catalog (Pâris et al. 2018) using a convolutional neural net trained with synthetic spectra (Dabbieri et al. 2020, Dabbieri et al. in prep.), and from visual inspection. The redshift range of the objects was principally between  $\sim 0.7$  and 1.0; several of the objects with redshifts smaller than z=0.75 are well-known FeLoBALQs (FBQS J104459.5+365605, FBQS J1214+2803, de Kool et al. 2001, 2002). The resulting sample included thirty objects that had spectra of sufficient quality to analyze both the BAL absorption at the short wavelength end and the H $\beta$  and [O III] emission at the long wavelength end. The other twenty objects analyzed by Choi et al. (2022) had too high redshift to include the rest-frame H $\beta$  and [O III] emission at the long-wavelength end. The spectra of five example FeLoBALQs from the

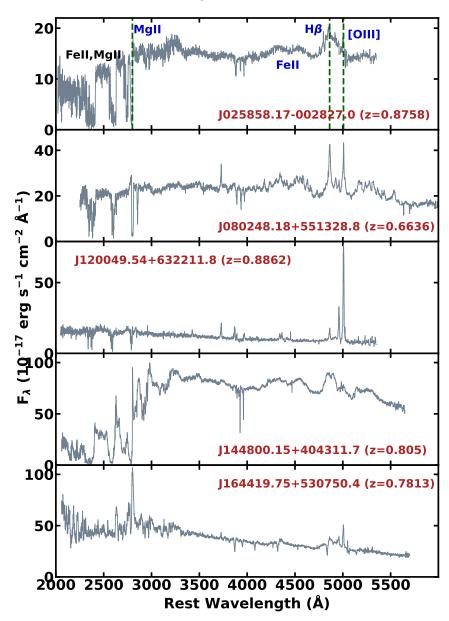


Figure 1. The SDSS or BOSS spectra of five FeLoBALQs from our sample. The Fe II and Mg II absorption can be seen at short wavelengths, and the H $\beta$ , [O III], and Fe II complex is present at long wavelengths. The vertical dashed lines in the top line show the rest-frame wavelengths of Mg II, H $\beta$ , and the 5007Å component of [O III]. A wide range of absorption and emission morphologies can be seen. The optical-band spectra of the full sample are shown in Fig. 3, while the near-UV spectra (with SimBAL model fits) are found in Choi et al. (2022).

sample displayed in Fig. 1 illustrate the wide range of absorption line and emission line properties in the sample. The properties of the sample are presented in Table 1 of Choi et al. (2022).

The sample of thirty objects can be divided into three classes depending the origin of their BAL classification. Ten objects are classified as BAL quasars in the NASA/IPAC Extragalactic Database<sup>1</sup>.

 $<sup>^{1}</sup>$  NED: http://ned.ipac.caltech.edu

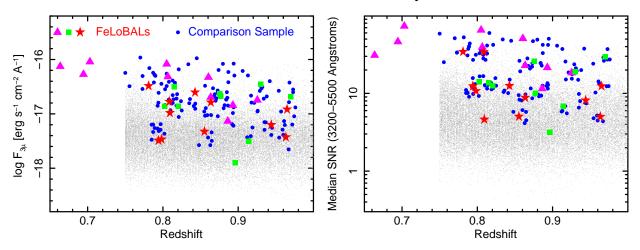


Figure 2. Distribution of the FeLoBAL quasar and comparison sample as a function of the comparison-sample matching properties: the  $3\mu m$  flux density, the redshift, and the median SNR in the rest frame 3200–5500Å bandpass. The FeLoBALQs are subdivided into objects classified as BAL quasars in NED (magenta triangles), objects included in the SDSS DR12 BAL catalog (green squares Pâris et al. 2017), and objects newly classified as BAL quasars (red stars). The redshift-selected parent sample, shown in grey, was drawn from the DR14 quasar catalog (Pâris et al. 2018). The three objects at low redshift are previously identified, well-known FeLoBAL quasars.

Nine more are included in the SDSS DR12 BAL quasar catalog (Pâris et al. 2017). The remaining eleven are newly classified as BAL quasars.

For comparison, we created a sample of unabsorbed quasars. Our goal was to identify five unabsorbed quasars from the SDSS DR14Q (Pâris et al. 2018) for each FeLoBAL quasar. For each FeLoBALQ, we selected a set of unabsorbed objects that lay near it in redshift, 3-micron luminosity density, and signal-to-noise ratio. Our criteria for proximity were  $\Delta \log F_{3\mu} = 0.3$ ,  $\Delta z = 0.01$ , and  $\Delta SNR = 0.1$ . Many quasar properties depend on luminosity; examples include the emission-line equivalent widths (Baldwin 1977) and BAL velocity (e.g., Ganguly et al. 2007). BAL quasars tend to be reddened (e.g., Krawczyk et al. 2015), and evidence for reddening is present in this sample (Leighly et al. in prep.). Therefore, we use the 3-micron luminosity as representative, rather than the luminosity in the optical or UV. From those, we randomly chose 5 objects, visually inspecting each one to be sure that it was not a BALQ and had analyzable H $\beta$ /[O III] emission lines, i.e., the H $\beta$  line could be discerned by eye. Six objects had such high signal-to-noise ratios that this selection method yielded too few comparison objects. For those, the redshift criterion was relaxed. Finally, the three objects with the poorest signal-to-noise ratio did not yield sufficient analyzable comparison sample; regardless, we retained these objects in our FeLoBALQ sample. The result was a comparison sample of 132 unabsorbed quasars. The distribution of the sample properties is shown in Fig. 2.

## 2.2. Optical Band Modeling

Our goals for the optical-band modeling were to fine tune the redshifts (necessary to measure the outflow velocities), extract the H $\beta$  properties to estimate the black hole mass, and extract the [O III] and Fe II properties. We modeled the optical-band spectra using Sherpa<sup>2</sup> (Freeman et al. 2001).

<sup>&</sup>lt;sup>2</sup> https://sherpa.readthedocs.io/en/latest/

Although intended for spectral fitting in the X-ray band, Sherpa has more than sufficient flexibility and robustness to fit optical spectra.

In order to take into account potential covariance between emission lines, continuum, and the Fe II pseudo-continuum, we modeled all components simultaneously. Most of the spectra were modeled between 3550Å and 5500Å. Some Seyfert 1.5 and 1.8 objects were modeled down to 3300Å to include the [Ne V] lines. Sometimes the long-wavelength limit was as low as 5200Å for higher-redshift objects due to the long wavelength limit of the SDSS/BOSS spectrograph.

Estimating the redshift from optical emission lines is known to be difficult because many lines show evidence for outflows. Following the discussion in Zakamska & Greene (2014), we usually used the lowest ionization narrow line available to estimate the redshift. When H $\beta$  could be clearly distinguished from broad H $\beta$ , we used that. Narrow H $\beta$  was fit in 16 out of 30 of the spectra. Most commonly, we used [O II] $\lambda$ 3727, which was present in 27 out of 30 of the spectra. When neither line was available, the SDSS DR14 redshift was used, or the redshift was estimated from the shape of the near-UV Fe II emission.

The continuum under the H $\beta$  and [O III] lines was modeled using a power law. In some cases, we observed an upturn of the spectrum towards shorter wavelengths. We modeled that upturn with either a recombination continuum model or a broken power law model.

Most frequently, we modeled the Fe II emission using the line lists developed from the strong-Fe II Seyfert galaxy I Zw 1 (Véron-Cetty et al. 2004). In a few cases, the Fe II emission is very prominent and complex, and we used the more flexible Fe II model constructed by Kovačević et al. (2010). This model is comprised of five line lists, three of which correspond to different lower levels of the transitions. This model only spans 4400–5500Å, and we modeled the 3550–4400Å region using the Véron-Cetty et al. (2004) model, fitting both segments of the spectrum simultaneously.

The Balmer lines (H $\beta$ , H $\gamma$ , H $\delta$ , H $\epsilon$ ) were modeled using either a single Lorentzian profile, a single Gaussian profile, or two Gaussians. When a cusp could be seen in the H $\beta$  profile, the broad lines were modeled with Gaussians, and a set of narrow Gaussian lines were included to model the narrow Balmer emission. There should be a contribution to the H $\beta$  profile from the narrow-line region, but we did not model it unless a cusp was present. We experimented with including a narrow H $\beta$  component with width and position tied to the [O III] lines and an intensity one tenth of the [O III] emission (Cohen 1983), and found that the measurements of H $\beta$  agreed within the error bars with the results of models that include a scaled narrow component. The 2-broad-Gaussian profile was only required for a few objects, and was most frequently used when the H $\beta$  line appeared to have a red wing.

We modeled the [O III] lines with either one or two pairs of Gaussian profiles. As usual, the 4959Å component was constrained to have the same width, 2.92 times the intensity, and lie a fixed wavelength ratio from the 5007Å component. In most cases, the preferred model used two pairs of lines; however, one pair was used when the line was particularly weak (especially when Fe II was strong).

Several objects (J1030+3120, J1044+3656, J1214+2803, J1448+4043) were particularly challenging to model because of a combination of good signal-to-noise ratio, strong Fe II, and weak [O III]. One of the complicating factors is that we measured statistically significant blueshifts in the Fe II emission in J1214+2803 and J1448+4043 (by 330 and 740 km s<sup>-1</sup>, respectively). While the cosmological redshift of J1448+4043 remains uncertain because there are no low-ionization NLR reference lines, [O II] was

observed in the J1214+2803 spectrum, and the redshift could be measured securely. To measure the emission-line properties of these four objects, we assumed that they are physically similar, and then used the values of the parameters that could be measured in some objects to model other objects. Specifically, [O III] could be fully constrained by a single pair of gaussians in position, intensity, and width in both J1030+3120 and J1044+3656. The [O III] was too obscured to be fully constrained in J1214+2803 and J1448+4043. The median value of the [O III] FWHM for J1030+3120 and J1044+3656 was approximately  $2000 \, \mathrm{km} \, \mathrm{s}^{-1}$ . So for J1214+2803 and J1448+4043, the FWHM was fixed at that value, and the intensity and position were modeled. The plots of the spectra and their model fits are given in Fig. 3. The measured values of emission-line parameters are given in Table 1.

In some objects, the Fe II and/or [O III] emission was weak. We used the F test (Bevington 1969) to gauge the statistical signficance of these parameters in each model for both the FeLoBAL quasar and comparison sample. We used a significance cutoff of p = 0.05. We found that 40 and 15 (30% and 50%) of the comparison and FeLoBALQ sample did not statistically require the Fe II emission. We found that 12 and 8 (16% and 27%) of the comparison and FeLoBALQ sample did not statistically require the [O III] emission.

No stellar population was apparent in the spectra of most of the FeLoBAL and comparison sample objects, so we did not include a young stellar population in our model. We reasoned that because the signal-to-noise ratio of many of our spectra is low, an additional continuum component could not be robustly constrained. Not including this component, assuming that it is present in some objects, adds scatter to the equivalent widths and velocity width of both the FeLoBALQ and comparison samples.

Several emission-line properties were derived from the optical-model-fitting results; these are compiled in Table 1 for the FeLoBAL quasars. The total [O III] luminosity was computed from the [O III] $\lambda$ 5007 line flux alone. We computed the parameter R<sub>FeII</sub>, commonly defined as the ratio of the Fe II equivalent width between 4434–4684 Å to the broad H $\beta$  equivalent width. We followed the methodology of Zakamska & Greene (2014) to extract the [O III] median velocity offset  $v_{50}$  and velocity width  $w_{80}$ . Briefly, from the normalized cumulative function of the broad H $\beta$  model profile, the velocities at 0.1, 0.5, and 0.9 were identified. The velocity at 0.5 is assigned to  $v_{50}$ , and  $w_{80}$  is the difference between the velocities at 0.1 and 0.9. It is important to note that, unlike Zakamska & Greene (2014) and similar studies of obscured quasars, the quality of these measurements varied dramatically through our sample, and are not very robustly measured in objects with very strong Fe II and weak [O III].

We estimated the bolometric luminosity using the estimate of the rest-frame flux density at 3 microns and the bolometric correction derived by Gallagher et al. (2007). This bolometric correction was derived from 259 quasars with 0.14 < z < 5.22 and estimated log bolometric luminosities  $45.1 < \log L_{\rm Bol} < 47.4$  [erg s<sup>-1</sup>] with a median value of 46.4. Our estimated bolometric luminosities fall between  $45.1 < \log L_{\rm Bol} < 46.2$  with a median value of 46.2. Although our objects are somewhat less luminous than the quasars considered by Gallagher et al. (2007), the difference in median is only 0.2 dex. We obtained the 3-micron flux density from the WISE photometry by doing a log-linear interpolation. For objects in this redshift range (0.7–0.97), 3 microns falls near the W2 effective wavelength (4.6 microns), and generally the W2 magnitude was measured with good signal-to-noise ratio in this sample of relatively nearby objects.

The black hole mass estimate requires an estimate of the radius of the H $\beta$ -emitting broad-line region. We used the formalism given by Bentz et al. (2006). The flux density at 5100Å was calculated from the power-law model component of the emission-line model fits, and then used to estimate the radius of the H $\beta$  emitting region. We did not correct for reddening intrinsic to the quasar, and therefore objects with significantly-reddened spectra will have somewhat underestimated black hole masses. The black hole mass was estimated using the FWHM of the H $\beta$  line and following the formalism of Collin et al. (2006). In particular, we used their Eq. 7 to estimate the scale factor f based on the FWHM of the H $\beta$  line.

We calculated the size of the 2800Å continuum emission region using the estimated black hole mass and the bolometric luminosity and the procedure described in § 6.1 of Leighly et al. (2019). To summarize, we used a simple sum-of-blackbodies accretion disk model (Frank et al. 2002) and assigned the 2800Å radius to be the location where the radially-weighted brightness dropped by a factor of e from the peak value. This estimate may not be accurate for the full range of Eddington ratios represented by the sample, since structure of the accretion disk is thought to be different for very low and very high accretion rates (e.g., Giustini & Proga 2019).

The uncertainties in the derived parameters were estimated using the Sherpa model fit errors. Because the errors produced by Sherpa were sometimes asymmetric, we used a Monte Carlo scheme to propagate errors. Specifically, we created 10,000 instances of each parameter varying the value within the errors, then computed the derived property, and extracted the  $1\sigma$  errors from the cumulative distributions.

We investigated whether there are any systematic differences in the properties measured in this paper between the previously-classified and the newly-classified BAL quasars using two-sample Kolmogorov-Smirnov (KS) test and the two-sample Anderson-Darling (AD) test. Among those seventeen properties, we found significant (p < 0.05) differences in only three properties. The SPCA Eigenvector 4 coefficient (§2.3) was lower in the new objects. Examining the plot of the PCA eigenvectors (Fig. 4) shows that this means that objects with narrow Fe II emission lines are preferentially represented among the previously-identified objects. The median bolometric luminosity was 0.44 dex lower among the new FeLoBAL quasars compared with the previously-known objects. This reflects the fact that the brightest objects in a sample are usually identified first, likely because they have higher signal-to-noise ratio spectra. Finally, the size of the 2800Å emission region of the new objects 0.1 dex lower than the previously-known objects, likely a consequence of the lower luminosities.

The 132 comparison-sample spectra were subjected to the same analysis.

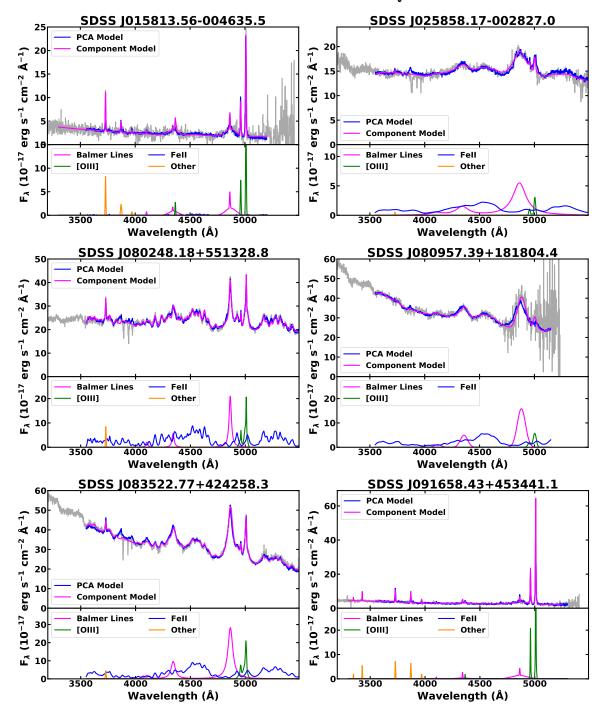


Figure 3. The optical portion of the FeLoBAL sample spectra overlaid with the best-fitting model spectrum. Both the component-based emission-line (§2.2) and the principal component eigenvector (§2.3) model fits are shown. The lower panel shows the components from the component-based model.

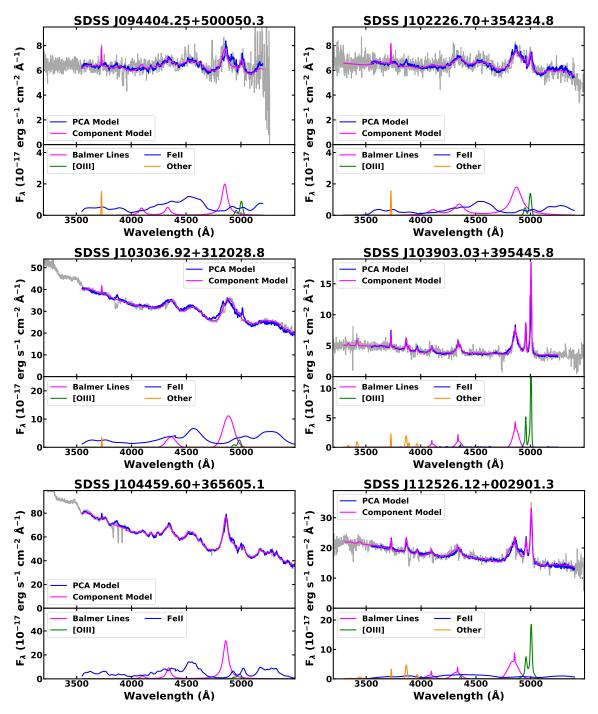


Figure 3. Continued.

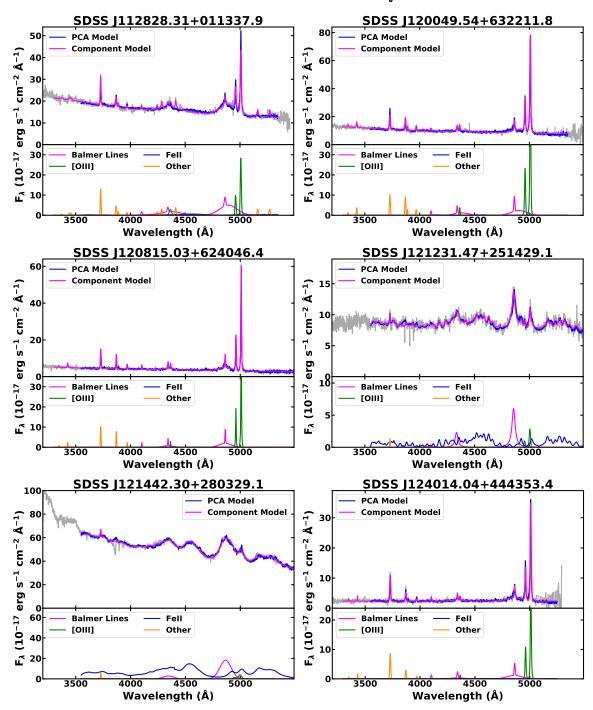


Figure 3. Continued.

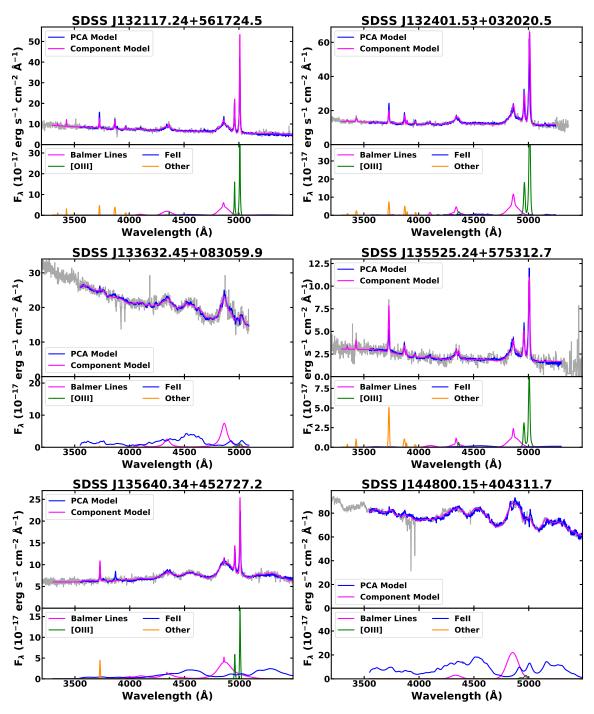


Figure 3. Continued.

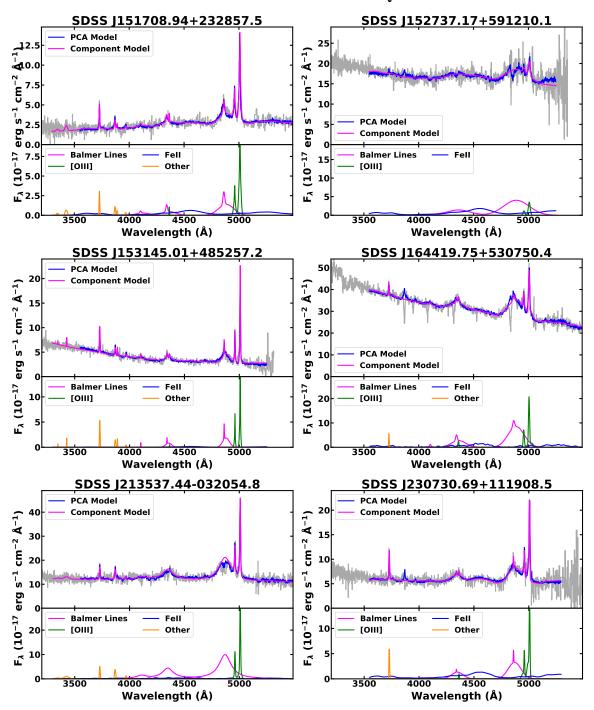


Figure 3. Continued.

 Table 1. Spectral Fitting Results

SDSS Object Name	Hβ FWHM	Hβ EW	$R_{ m FeII}$	[O III] EW	[O III] V <sub>50</sub>	[O III] W <sub>80</sub>	[O III] Luminosity	$\log L_{ m Bol}$	BH Mass	Edd. Ratio	E1 Parameter a
SDSS Object Name	,	11ρ Ενν	rtFeII	. ,		. ,	. ,		BII Wass	Edd. Ratio	El l'arameter
	$(\mathrm{km}\mathrm{s}^{-1})$	(Å)		(Å)	$(\mathrm{km}\mathrm{s}^{-1})$	$(\mathrm{km}\mathrm{s}^{-1})$	$(\mathrm{erg}\mathrm{s}^{-1})$	$(\mathrm{erg}\mathrm{s}^{-1})$	$({ m M}_{\odot})$		
015813.56 - 004635.5	$6850^{+1180}_{-700}$	$93^{+18}_{-9.8}$	$0.196^{+0.115}_{-0.076}$	$106.5^{+4.2}_{-3.8}$	$67^{+9}_{-8}$	$530^{+20}_{-20}$	$42.87^{+0.02}_{-0.02}$	$45.11 \pm 0.11$	$8.57^{+0.13}_{-0.11}$	$-1.56^{+0.13}_{-0.11}$	$-2.45^{+0.39}_{-0.42}$
025858.17 - 002827.0	$9000^{+290}_{-290}$	$96^{+3.1}_{-3.2}$	$0.378^{+0.045}_{-0.039}$	$4.3^{+0.5}_{-0.5}$	$-261^{+58}_{-52}$	$1110^{+160}_{-140}$	$42.32_{-0.06}^{+0.05}$	$46.36\pm0.01$	$8.64^{+0.04}_{-0.05}$	$-0.38^{+0.04}_{-0.05}$	$1.10^{+0.16}_{-0.14}$
080248.18 + 551328.8	$1560^{+30}_{-30}$	$42^{+0.5}_{-0.6}$	$1.67^{+0.045}_{-0.045}$	$17.8^{+0.6}_{-0.6}$	$-111^{+21}_{-23}$	$1670^{+60}_{-60}$	$42.82^{+0.01}_{-0.01}$	$46.56 \pm 0.009$	$7.57^{+0.04}_{-0.04}$	$0.9^{+0.04}_{-0.04}$	$1.01^{+0.039}_{-0.037}$
080957.39 + 181804.4	$5400^{+140}_{-150}$	$56^{+1.7}_{-1.8}$	$0.743^{+0.069}_{-0.062}$	$9_{-1.0}^{+0.9}$	$-320^{+140}_{-182}$	$2180_0^{+0}$	$42.99^{+0.04}_{-0.05}$	$46.41 \pm 0.02$	$7.97^{+0.04}_{-0.04}$	$0.35^{+0.04}_{-0.04}$	$0.98^{+0.13}_{-0.12}$
083522.77 + 424258.3	$3250^{+40}_{-40}$	$91^{+0.8}_{-0.9}$	$0.696^{+0.017}_{-0.018}$	$22.9_{-0.7}^{+0.7}$	$-274^{+21}_{-21}$	$2100^{+80}_{-90}$	$43.18^{+0.01}_{-0.01}$	$46.58 \pm 0.01$	$8.33^{+0.04}_{-0.04}$	$0.15^{+0.04}_{-0.04}$	$0.05 \pm 0.04$
091658.43 + 453441.1	$10390^{+1200}_{-700}$	$102^{+12.}_{-7.8}$	$0.121^{+0.068}_{-0.107}$	$175.9^{+20.8}_{-21.4}$	$36^{+4}_{-6}$	$460^{+60}_{-40}$	$43.22^{+0.05}_{-0.05}$	$45.53 \pm 0.03$	$8.9^{+0.10}_{-0.07}$	$-1.47^{+0.1}_{-0.07}$	$-3.33^{+0.44}_{-0.67}$
094404.25 + 500050.3	$3800^{+620}_{-520}$	$35^{+4.7}_{-4.0}$	$1.308^{+0.262}_{-0.232}$	$4.9^{+1.3}_{-1.2}$	$-245^{+221}_{-225}$	$1840^{+470}_{-440}$	$42.1_{-0.12}^{+0.1}$	$46.17\pm0.02$	$8.46^{+0.13}_{-0.15}$	$-0.39^{+0.13}_{-0.15}$	$2.02^{+0.32}_{-0.27}$
102226.70 + 354234.8	$7360^{+740}_{-670}$	$59^{+5.4}_{-5.0}$	$0.538^{+0.11}_{-0.10}$	$6.8^{+0.9}_{-0.9}$	$-537^{+75}_{-82}$	$1630^{+290}_{-260}$	$42.08^{+0.06}_{-0.06}$	$46.05\pm0.02$	$8.66^{+0.09}_{-0.10}$	$-0.7^{+0.09}_{-0.10}$	$0.97 \pm 0.21$
103036.92 + 312028.8	$7090^{+110}_{-90}$	$53^{+2.0}_{-0.7}$	$0.868^{+0.056}_{-0.04}$	$4^{+0.4}_{-0.4}$	$-1581^{+76}_{-71}$	$2130^{+140}_{-140}$	$42.51_{-0.05}^{+0.04}$	$46.64 \pm 0.01$	$8.57 \pm -0.04$	$-0.02\pm0.04$	$1.86^{+0.12}_{-0.09}$
103903.03 + 395445.8	$3930^{+140}_{-170}$	$58 \pm 2.0$	$0.075^{+0.091}_{-0.078}$	$63^{+4.9}_{-5.2}$	$-252_{-26}^{+25}$	$1250^{+130}_{-120}$	$42.91^{+0.03}_{-0.04}$	$46.18\pm0.02$	$8.44^{+0.05}_{-0.06}$	$-0.35^{+0.05}_{-0.06}$	$-2.76^{+0.72}_{-0.65}$
104459.60 + 365605.1	$3460^{+30}_{-40}$	$57^{+0.4}_{-0.5}$	$0.832^{+0.018}_{-0.017}$	$4.0^{+0.3}_{-0.2}$	$-1405^{+83}_{-108}$	$2620^{+250}_{-190}$	$42.57 \pm 0.03$	$46.71 \pm 0.009$	$7.82 \pm 0.03$	$0.8 \pm 0.03$	
112526.12 + 002901.3	$6800^{+140}_{-130}$	$46^{+0.9}_{-0.8}$	$0.452^{+0.013}_{-0.019}$	$36.8^{+0.9}_{-1.0}$	$-344^{+27}_{-22}$	$2920^{+210}_{-170}$	$43.27 \pm 0.01$	$46.28\pm0.02$	$8.67 \pm 0.05$	$-0.48\pm0.05$	$1.83 \pm 0.06$ E $-0.76^{+0.03}_{-0.04}$ G $-1.57^{+0.39}_{-0.46}$ H $3.03^{+0.45}$
112828.31 + 011337.9	$11550^{+1160}_{-360}$	$70^{+8.7}_{-2.1}$	$0.125^{+0.064}_{-0.056}$	$27.9_{-4.3}^{+4.5}$	$-42^{+38}_{-20}$	$830^{+380}_{-90}$	$43.15 \pm 0.07$	$46.17\pm0.02$	$8.29^{+0.08}_{-0.05}$	$-0.22^{+0.08}_{-0.05}$	$-1.57^{+0.39}_{-0.46}$ $\Xi$
120049.54 + 632211.8	$10060^{+730}_{-680}$	$47^{+4.6}_{-4.2}$	$0.091^{+0.062}_{-0.051}$	$99.3^{+7.4}_{-7.6}$	$2^{+8}_{-10}$	$790^{+50}_{-40}$	$43.5 \pm 0.03$	$45.89 \pm 0.02$	$8.3 \pm 0.07$	$-0.53\pm0.07$	$-3.03_{-0.56}$
120815.03 + 624046.4	$8140^{+420}_{-330}$	$78^{+3.4}_{-2.9}$	$0.093^{+0.045}_{-0.046}$	$144.9^{+10.7}_{-10.6}$	$-11^{+6}_{-3}$	$590 \pm 40$	$43.13 \pm 0.03$	$45.42\pm0.04$	$8.31 \pm 0.05$	$-0.99\pm0.05$	$-3.37^{+0.34}_{-0.49}$
121231.47 + 251429.1	$2100\pm120$	$42.0\pm1.8$	$1.102^{+0.111}_{-0.103}$	$5.6^{+0.6}_{-0.5}$	$-240\pm34$	$900^{+140}_{-120}$	$42.16 \pm 0.04$	$46.34 \pm 0.01$	$7.99^{+0.06}_{-0.07}$	$0.25^{+0.06}_{-0.07}$	$1.76 \pm 0.12 \ge$
121442.30 + 280329.1	$7480 \pm 90$	$56 \pm 0.7$	$1.112^{+0.045}_{-0.042}$	$3.8 \pm 0.3$	$-657^{+103}_{-123}$	2180	$42.47^{+0.03}_{-0.04}$	$46.47 \pm 0.01$	$8.27 \pm 0.03$	$0.1 \pm 0.03$	$2.14^{+0.09}_{-0.08}$
124014.04 + 444353.4	$10050^{+1330}_{-1020}$	$87^{+11.0}_{-9.9}$	$0.083^{+0.065}_{-0.084}$	$162.4^{+23.0}_{-23.6}$	$86^{+17}_{-12}$	$790^{+100}_{-70}$	$43.25^{+0.06}_{-0.07}$	$45.66\pm0.03$	$8.49^{+0.11}_{-0.10}$	$-0.92^{+0.11}_{-0.10}$	$-3.56^{+0.55}_{-0.65}$
132117.24 + 561724.5	$6600^{+200}_{-150}$	$74^{+2.0}_{-2.1}$	$0.156^{+0.015}_{-0.06}$	$75.1^{+2.4}_{-2.1}$	$5^{+4}_{-5}$	$720\pm20$	$43.09 \pm 0.01$	$45.39 \pm 0.04$	$8.49^{+0.05}_{-0.04}$	$-1.2^{+0.05}_{-0.04}$	$-2.31^{+0.08}_{-0.40}$
132401.53 + 032020.5	$7360^{+330}_{-310}$	$60^{+2.2}_{-2.1}$	$0.168^{+0.055}_{-0.046}$	$81^{+8.0}_{-8.1}$	$165^{+12}_{-15}$	$1200^{+80}_{-60}$	$43.61^{+0.04}_{-0.05}$	$46.30\pm0.02$	$8.3 \pm 0.05$	$-0.1\pm0.05$	$-2.33^{+0.26}_{-0.27}$
133632.45 + 083059.9	$4240^{+170}_{-330}$	$48^{+1.4}_{-3.2}$	$0.999^{+0.090}_{-0.091}$	$2.6\pm0.5$	$9_{-90}^{+1715}$	2180	$42.05^{+0.08}_{-0.10}$	$46.1 \pm 0.01$	$8.21^{+0.05}_{-0.08}$	$-0.2^{+0.05}_{-0.08}$	$2.39^{+0.22}_{-0.20}$
135525.24 + 575312.7	$7560^{+680}_{-650}$	$97^{+7.3}_{-6.2}$	$0.24^{+0.039}_{-0.239}$	$104.1^{+8}_{-12.4}$	$-45^{+20}_{-82}$	$1320^{+1380}_{-120}$	$42.78^{+0.03}_{-0.05}$	$45.63 \pm 0.03$	$8.47^{+0.08}_{-0.09}$	$-0.93^{+0.08}_{-0.09}$	$-2.26^{+0.18}_{-0.67}$
135640.34 + 452727.2	$9540^{+990}_{-900}$	$140^{+24}_{-20}$	$0.57^{+0.16}_{-0.13}$	$27.5 \pm 3.4$	$-110^{+12}_{-11}$	$640^{+56}_{-50}$	$42.67^{+0.05}_{-0.06}$	$46.03\pm0.01$	$8.90^{+0.09}_{-0.10}$	$-0.96^{+0.10}_{-0.09}$	$-0.29^{+0.25}_{-0.23}$
144800.15 + 404311.7	$7670 \pm 100$	$44^{+0.6}_{-0.5}$	$1.196\pm0.033$	$1.6\pm0.2$	$-2084^{+120}_{-99}$	2180	$42.49 \pm 0.05$	$46.81\pm0.009$	$8.55 \pm 0.04$	$0.16 \pm 0.04$	$3.00 \pm 0.11$
151708.94 + 232857.5	$10080^{+1170}_{-640}$	$110^{+10}_{-6.0}$	$0.53^{+0.05}_{-0.1}$	$70.5^{+3.1}_{-3.0}$	$48^{+14}_{-12}$	$1320^{+60}_{-90}$	$42.72\pm0.02$	$45.92\pm0.02$	$9.02^{+0.1}_{-0.07}$	$-1.2^{+0.1}_{-0.07}$	$-1.24^{+0.08}_{-0.18}$
152737.17 + 591210.1	$16790^{+1170}_{-1080}$	$78^{+8.7}_{-7.8}$	$0.32^{+0.049}_{-0.062}$	$5.4\pm1$	$-30^{+78}_{-77}$	$1330^{+220}_{-210}$	$42.52\pm0.08$	$46.60\pm0.01$	$9.28 \pm 0.07$	$-0.78\pm0.07$	$0.76^{+0.21}_{-0.24}$
153145.01 + 485257.2	$4460^{+340}_{-350}$	$39 \pm 3.2$	$0.239^{+0.057}_{-0.201}$	$52.3^{+3.9}_{-4.4}$	$-10^{+11}_{-15}$	$640^{+120}_{-60}$	$42.82^{+0.03}_{-0.04}$	$45.86\pm0.02$	$8.67^{+0.08}_{-0.09}$	$-0.9^{+0.08}_{-0.09}$	$-1.62^{+0.21}_{-0.65}$
164419.75 + 530750.4	$10590^{+290}_{-160}$	$54^{+1.3}_{-0.9}$	$0.176^{+0.043}_{-0.020}$	$12.2^{+0.5}_{-0.7}$	$-79^{+17}_{-27}$	$1730^{+290}_{-420}$	$42.95^{+0.02}_{-0.03}$	$46.38\pm0.009$	$8.97^{+0.05}_{-0.04}$	$-0.69^{+0.05}_{-0.04}$	$-0.51^{+0.19}_{-0.11}$
213537.44 - 032054.8	$8270^{+380}_{-370}$	$185^{+5.2}_{-5.0}$	$0.038 \pm 0.01$	$33.2^{+1.7}_{-1.8}$	$5^{+13}_{-12}$	$870^{+110}_{-70}$	$43.06^{+0.02}_{-0.03}$	$46.41 \pm 0.01$	$8.75 \pm 0.06$	$-0.44\pm0.06$	$-2.74_{-0.27}^{+0.20}$
230730.69 + 111908.5	$8430^{+340}_{-280}$	$102^{+4.4}_{-3.2}$	$0.564^{+0.120}_{-0.104}$	$46.7^{+3.3}_{-3.7}$	$-174_{-31}^{+34}$	$1480^{+140}_{-170}$	$42.92^{+0.03}_{-0.04}$	$46.31\pm0.02$	$8.69 \pm 0.05$	$-0.47\pm0.05$	$-0.80\pm0.18$

 $<sup>^</sup>a{
m The}~E1$  parameter is defined in §3.1.

# 2.3. Principal Components Analysis

While spectral decomposition using emission-line profiles and templates is a widely used and valid approach, model dependence must be present. Decomposition using spectral principal components provides a complementary and less model dependent analysis.

We created the principal components using the 132 comparison spectra described in §2.1. We preprocessed the spectra by dividing by the fitted continuum flux density at 4950Å, and subtracting the scaled continuum obtained from spectral fitting. This procedure of subtracting the continuum differs from many applications of PCA (e.g., Shang et al. 2003; Pâris et al. 2011) and has the advantage that the considerable variance present due to variations in continuum slope does not contaminate the emission-line eigenvectors.

We used EMPCA (Bailey 2012) to compute the eigenvectors. This method has several advantages over the traditional singular value decomposition method. Principally, the method weights the data using the uncertainties, and missing data are given a weight of zero. This is important since PCA methods find the regions of the data that have the most variance, noise can infiltrate the eigenvectors that describe the most variance in the data set (e.g., Fig. 5 in Bailey 2012). The first and second eigenvectors modeled 29% and 9.9% of the variance, respectively. We retain the first five eigenvectors to model the variance of the emission lines; subsequent ones each model less than 1% of the variance. The mean and first five eigenvectors are shown in Fig. 4.

The mean spectrum and eigenvectors offer no great surprises. The first eigenvector shows the strong anticorrelation between [O III] and Fe II, and is essentially the Boroson & Green (1992) first eigenvector. This construct is historically known as Eigenvector 1, and is repeatedly found in PCA analysis of optical rest-frame quasar spectra (e.g., Sulentic et al. 2000; Grupe 2004; Ludwig et al. 2009; Wolf et al. 2020). The second eigenvector shows strong Balmer lines and Fe II emission. The fourth eigenvector is interesting because it includes very narrow Fe II lines, and therefore should be strongly negative when modeling the narrow-line Seyfert 1 galaxies in our sample. It is notable that the [O II] line and other very narrow lines are clearly present in the spectra; this is a consequence of the careful redshift correction.

We used the mean spectrum and first five eigenvectors to fit the 30 FeLoBAL spectra and the 132 comparison sample spectra. The spectra were prepared for spectral fitting by being normalized by the same value used to process the spectra for PCA analysis. The model is comprised of a linear combination of the same continuum model used for each spectrum in §2.2, the mean emission-line spectrum, and the five eigenvectors, where the normalization of the mean emission-line spectrum is frozen at a value of 1. The continuum normalization was left free to vary, as were the coefficients of the eigenvectors which serve to modify the shape of the mean emission line spectrum.

# 3. DISTRIBUTION COMPARISONS AND CORRELATIONS

In this section, we compare the emission-line properties of the FeLoBAL quasars with those of the comparison sample of unabsorbed quasar using cumulative distribution plots. We then examine relationships among the optical and global parameters using Spearman-rank correlations.

# 3.1. Distributions

We report the results of the two-sample Kolmogorov-Smirnov (KS) test and the two-sample Anderson-Darling (AD) test in Table 2. The KS test reliably tests the difference between two distributions when the difference is large at the median values, while the AD test is more reliable if the

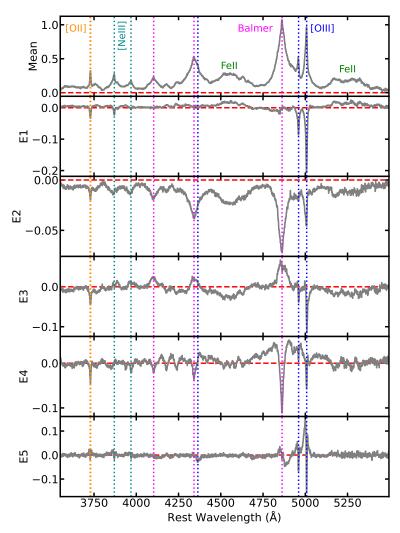


**Figure 4.** The mean spectrum and first five eigenvectors constructed from the 132 objects in the comparision sample. Principal emission lines are labeled.

differences lie toward the maximum or minimum values (i.e., the median can be the same, and the distributions different at larger and smaller values)<sup>3</sup>. We also examined the relationships among the optical properties of our sample of FeLoBALQs and of the comparison sample. The four pairs of columns in the table correspond to several different cases. The first pair gives the results for all the data; the remainder are divided by the E1 parameter which is described next.

<sup>&</sup>lt;sup>3</sup> E.g., https://asaip.psu.edu/articles/beware-the-kolmogorov-smirnov-test/

Table 2. Parameter Distributions Comparison

Parameter Name		FeLoBALQs						
	All (30/132)		E1< 0 (	17/61)	E1> 0	(13/71)	E1< 0 vs E1> $0^{a}$	
	$_{ m KS}b$	$^{\mathrm{AD}}{}^{\mathcal{C}}$	$_{ m KS}b$	$_{\mathrm{AD}}c$	$_{ m KS}b$	$_{\mathrm{AD}}c$	$_{ m KS}b$	$_{\mathrm{AD}}c$
Hβ FWHM	$0.56/1.5  imes 10^{-7}$	18.0/ < 0.001	$0.65/6.3  imes 10^{-6}$	13.3/ < 0.001	0.42/0.029	4.25/6.5  imes 10-3	0.43/0.09	3.3/0.014
$_{\mathrm{H}\beta}\;\mathrm{EW}$	0.25/0.088	0.99/0.13	0.24/0.37	0.19/ > 0.25	0.37/0.068	1.1/0.12	0.48/0.050	2.65/0.027
$R_{ m FeII}$	$0.35/3.6  imes 10^{-3}$	$4.5/5.4  imes 10^{-3}$	$0.60/4.9 \times 10^{-5}$	7.3/<0.001	0.14/0.97	-0.83/ > 0.25	$0.77/6.8  imes 10^{-5}$	11.8/<0.001
[O III] EW	0.28/0.034	$6.5/1.0  imes 10^{-3}$	$0.47/3.0  imes 10^{-3}$	8.0/<0.001	$0.61/2.1 \times 10^{-4}$	8.3/<0.001	$0.94/2.3  imes 10^{-7}$	14.1/ < 0.001
$[{ m O~{\sc iii}}]~V_{50}~({ m km~s^{-1}})$	0.25/0.084	1.8/0.056	$0.44/6.8  imes 10^{-3}$	$5.3/2.7  imes 10^{-3}$	0.29/0.26	1.25/0.10	$0.67/1.2  imes 10^{-3}$	7.3/<0.001
${ m [O~{\sc iii}]~W_{80}~(km~s^{-2})}$	0.15/0.61	-0.50/ > 0.25	0.40/0.021	<b>2.4</b> /0.032	0.40/0.040	2.0/0.050	$0.67/1.2  imes 10^{-3}$	7.5/ < 0.001
SPCA E1	$0.33/7.2  imes 10^{-3}$	$5.0/3.5  imes 10^{-3}$	$0.53/6.0  imes 10^{-4}$	9.8/<0.001	0.38/0.062	2.0/0.048	$1.0/1.7  imes 10^{-8}$	14.8/<0.001
SPCA E2	$0.40/4.7  imes 10^{-4}$	$5.1/3.1  imes 10^{-3}$	0.21/0.53	-0.64/>0.25	$0.66/4.8  imes 10^{-5}$	8.4/ < 0.001	0.48/0.050	2.7/0.026
SPCA E3	$0.37/1.5  imes 10^{-3}$	10.3/<0.001	$0.63/1.3  imes 10^{-5}$	10.9/<0.001	0.39/0.048	1.3/0.09	$0.69/8.0  imes 10^{-4}$	$5.5/2.3  imes 10^{-3}$
SPCA E4	0.14/0.70	-0.14/ > 0.25	0.38/0.032	3.0/0.020	0.35/0.10	1.2/0.10	0.55/0.014	3.6/0.011
E1 Parameter	$0.34/4.7  imes 10^{-3}$	$5.7/1.9  imes 10^{-3}$	$0.57/1.6  imes 10^{-4}$	9.0/<0.001	$0.49/6.9  imes 10^{-3}$	$5.0/3.4  imes 10^{-3}$	$1.0/1.7  imes 10^{-8}$	14.8/<0.001
${\rm H}\beta$ FWHM Deviation	$0.33/7.9  imes 10^{-3}$	6.8/<0.001	0.36/0.050	3.0/0.019	0.42/0.026	3.5/0.012	0.34/0.29	0.26/ > 0.25
[O III] Luminosity	0.17/0.41	-0.07/ > 0.25	0.25/0.33	0.48/0.21	0.25/0.43	-0.58/ > 0.25	$0.77/6.8  imes 10^{-5}$	9.0/<0.001
$ m M_{BH}$	0.12/0.79	-0.67/>0.25	0.31/0.12	0.91/0.14	0.27/0.32	0.88/0.14	$0.59/6.0  imes 10^{-3}$	$5.5/2.2  imes 10^{-3}$
$\mathcal{L}_{\mathrm{Bol}}$	0.11/0.91	-0.72/ > 0.25	0.31/0.12	1.65/0.068	$0.47/9.0  imes 10^{-3}$	3.6/0.011	$0.65/1.7  imes 10^{-3}$	8.5/<0.001
$\rm L_{Bol}/L_{Edd}$	0.20/0.23	3.1/0.018	0.35/0.06	3.5/0.013	$0.50/4.2  imes 10^{-3}$	6.9/<0.001	$0.72/2.9  imes 10^{-4}$	9.7/<0.001
$R_{2800} [pc]$	0.16/0.48	0.16/ > 0.25	0.30/0.16	0.43/0.22	0.17/0.86	-0.76/ > 0.25	0.18/0.93	-0.77/ > 0.25

<sup>&</sup>lt;sup>a</sup> The optical data from the E < 0 (E > 0) FeLoBALQ subsamples include 17 (13) objects. The SimBAL data from the E1 < 0 (E1 > 0) subsamples include 19 (17) measurements because several objects have more than one outflow component.

<sup>&</sup>lt;sup>b</sup> The Kolmogorov-Smirnov Two-sample test. Each entry has two numbers: the first is the value of the statistic, and the second is the probability that the two samples arise from the same parent sample. Bold type indicates entries that yield p < 0.05.

<sup>&</sup>lt;sup>c</sup> The Anderson-Darling Two-sample test. Each entry has two numbers: the first is the value of the statistic, and the second is the probability that the two samples arise from the same parent sample. Note that the implementation used does not compute a probably larger than 0.25 or smaller than 0.001. Bold type indicates entries that yield p < 0.05.

The principal components analysis revealed that the dominant variance in the emission line properties arises from the anticorrelation between the [O III] and the Fe II (§2.3). As noted above, this anticorrelation is common among samples of optical spectra of quasars, and also appears among the UV emission lines and in other properties of quasars (e.g., Francis et al. 1992; Boroson & Green 1992; Brotherton et al. 1994; Corbin & Boroson 1996; Wills et al. 1999; Shang et al. 2003; Grupe 2004; Yip et al. 2004; Wang et al. 2006; Ludwig et al. 2009; Shen 2016). In this sample, we parameterize these properties using the [O III] equivalent width and the ratio of Fe II to H $\beta$  (hereafter referred to as  $R_{\text{FeII}}$ ; e.g., Shen & Ho 2014). The anticorrelation for the FeLoBALQs and comparison sample is seen in the left panel of Fig. 5.

We created a summary statistic parameter that describes the anticorrelation. We computed the base-10 logarithm of  $R_{FeII}$  and [O III]. For convenience, we computed the mean and standard deviation of both quantities from the comparison sample, and used those values to scale and normalized both samples. We then used the bivariate correlated errors and intrinsic scatter (BCES) method<sup>4</sup> (Akritas & Bershady 1996) to obtain the bisector of the two parameters. This method takes into account the uncertainty on both parameters. The bisector is more appropriate than a regression, since neither parameter can be identified as the dependent or independent variable. After scaling and normalization, the slope of the bisector is close to -1, as expected.

An alternative method for obtaining our summary statistic parameter takes into account the fact that [O III] and Fe II emission was not found to be statistically necessary using the F test (§2.2). We evaluated the bisector using the methodology of Isobe et al. (1990) taking into account the statistically unnecessary values as upper limits using the likelihood given by Sawicki (2012). The relationship is shown in Fig. 5. As expected, the bisector line is shifted slightly toward lower values of  $R_{\rm FeII}$  and [O III] equivalent width. Noting that the summary statistic is defined for convenience and does not represent a physical relationship, we proceeded with the original bisector because it appears more representative of the data.

We then rotated the coordinate system so that the long axis of the bisector is horizontal. The result is shown in the right panel of Fig. 5. We take the rotated X-axis value as our desired summary statistic, hereafter referred to as the "E1 parameter". Note that this parameter is closely related to the SPCA1 fit coefficients. As we will discuss in §3.3, the FeLoBALQs consist of two distinct populations simply divided at E1 = 0. In Table 2 we compare the FeLoBALQs with E1 < 0 and E1 > 0 with their unabsorbed sample counterparts, and with one another also.

# 3.2. FeLoBALQs versus Unabsorbed Objects 3.2.1. Optical Properties

The H $\beta$  emission line was parameterized using the FWHM and the equivalent width. The cumulative distributions of the H $\beta$  FWHM are plotted in Fig. 6. The cumulative distributions for the FeLoBALQs and comparison sample are profoundly different (see Table 2), with the FeLoBALQs showing consistently larger FWHM. There is a tendency for the FeLoBALQs to have smaller H $\beta$  equivalent widths, but it is not statistically significant.

<sup>&</sup>lt;sup>4</sup> https://github.com/rsnemmen/BCES

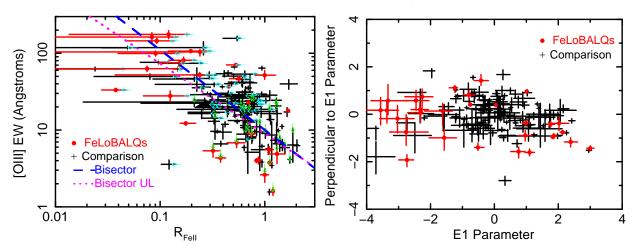


Figure 5. The construction of the E1 parameter. Left: The anticorrelation of the ratio of the Fe II and H $\beta$  fluxes with the [O III] equivalent width. Arrows mark the measurements deemed statistically insignificant using the F test (§2.2). The new coordinate system was defined by the bisector slope computed from the normalized and scaled log values of these parameters. The relationship is given by  $E1 = 0.679(\log_{10}(R_{\rm FeII}) + 0.270) - 0.735(\log_{10}([OIII]EW) - 1.288)$ . Right: The data after rotation to the new coordinate system. The bisector line now lies along the x axis and thereby defines the E1 parameter.

There is a statistically significant difference in the  $R_{FeII}$  between the comparison sample and the FeLoBALQs for the E1 < 0 subsample. There are excess low  $R_{FeII}$  objects among the FeLoBALQs, and a hint of excess high  $R_{FeII}$  objects as well. We will return to this point in §3.3.

We used the [O III] equivalent width to quantify the strength of the [O III] emission line, and  $v_{50}$  and  $w_{80}$  (defined in §2.2) to parameterize the profile shape. The distributions of the [O III] equivalent width are statistically significantly different; note that this is an excellent example of a pair of distributions that are found to be less significantly different using the KS test (p = 0.034) compared with the AD test (p < 0.001; the software that we used does not compute probabilities less than this value) due to the fact that the median of the distributions is not very different, but the ends are. Specifically, there are many more FeLoBALQs with much larger and much smaller [O III] equivalent widths than the comparison sample. There are no statistical differences between the FeLoBALQs and the comparison sample for  $v_{50}$  and  $w_{80}$ .

#### 3.2.2. The SPCA Eigenvector Coefficients

We compared the fit coefficients for the model using first five SPCA eigenvectors (§2.3) in Fig. 7, and the KS and AD statistics are given in Table 2. We found that the distributions for the FeLoBALQs differs from those of the comparison sample for the first three coefficients.

## 3.2.3. Global Properties

We investigated the distributions of several global properties of the quasars including the integrated [O III] luminosity, the bolometric luminosity, the black hole mass (computed as described in  $\S 2.2$ ), the Eddington ratio  $L_{Bol}/L_{Edd}$ , and the size of the 2800Å continuum emission region. The distributions are shown in Fig. 8 and the KS and AD statistics are given in Table 2. Most of these properties are statistically consistent between the FeLoBALQs and the comparison sample objects. The exception

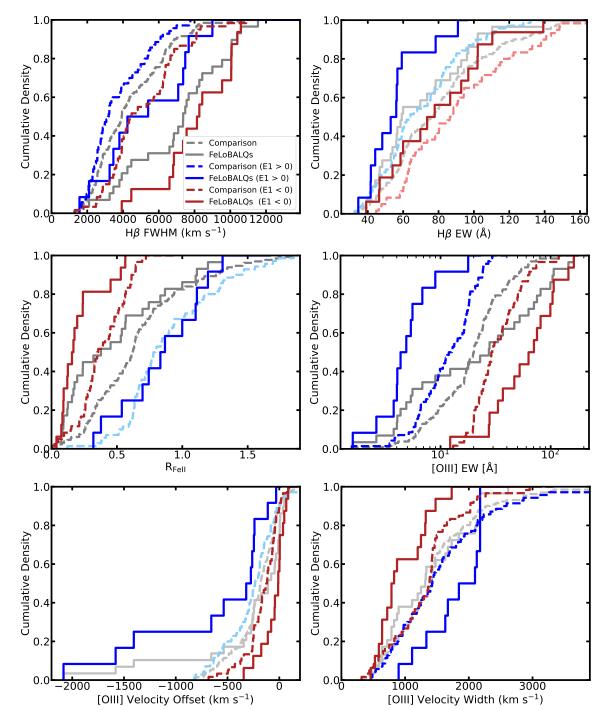
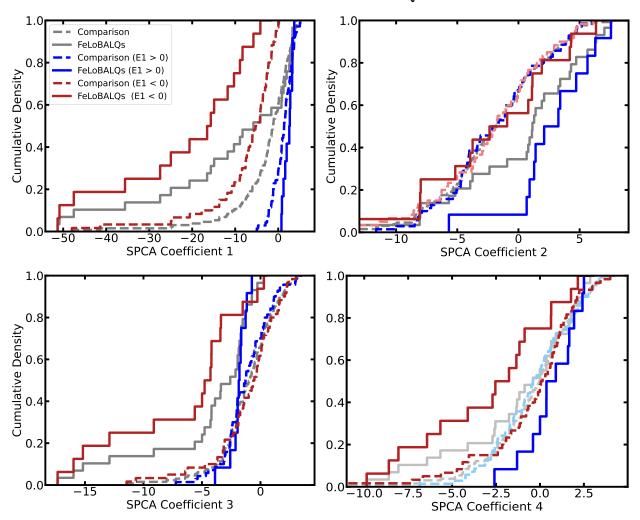


Figure 6. Cumulative distribution plots of the optical emission-line parameters. The data are sampled in three ways: the grey lines show the full FeLoBALQ and comparison samples, and the blue (red) lines sho the FeLoBALQ and comparison samples for E1 parameter E1 > 0 (E1 < 0); the E1 parameter is introduced in §3 and discussed in §3.3. The Kolmogorov-Smirnov and Anderson-Darling statistics for four different comparisons are given in Table 2. Distributions that are significantly different (p < 0.05) are shown in dark red, dark blue, or dark grey, while distributions that are not significantly different are shown in pale colors. The full sample distributions are statistically significantly different for Hβ FWHM, R<sub>FeII</sub>, and [O III] EW. The FeLoBALQs partitioned by the E1 parameter are statically significantly different for all properties.



**Figure 7.** Cumulative distribution plots of the SPCA fit coefficients. The colors and line styles are the same as in Fig. 6, and the Kolmogorov-Smirnov and Anderson-Darling statistics for four different comparisons are given in Table 2. The full sample distributions are statistically significantly different for the coefficients for the first three eigenvectors and are different for all four eigenvectors for the two populations of FeLoBALQs.

is the Anderson-Darling test for the Eddington ratio; the FeLoBALQs have an excess of objects at high and low  $\rm L_{Bol}/\rm L_{Edd}$  values.

# 3.3. Evidence for Two Populations of FeLoBAL Quasars

Examination of the right panel of Fig. 5 reveals that the FeLoBALQs are not distributed evenly in the E1 parameter. While the comparison sample objects distribution peaks at  $E1 \sim 0$ , declining toward lower and higher values, the FeLoBALQ E1 values straddle both sides of the center. The Kolmorogov-Smirnov (Anderson-Darling) tests yield a probability of 0.46% (0.19%) that the two samples were drawn from the same parent distribution. The differences in the distribution are visualized in the histogram and cumulative distributions shown in the top panel of Fig. 9.

The FeLoBAL E1 parameter distribution appears to be bimodal, but statistical tests do not establish bimodality. We first used the Hartigan & Hartigan (1985) dip test. This test could not

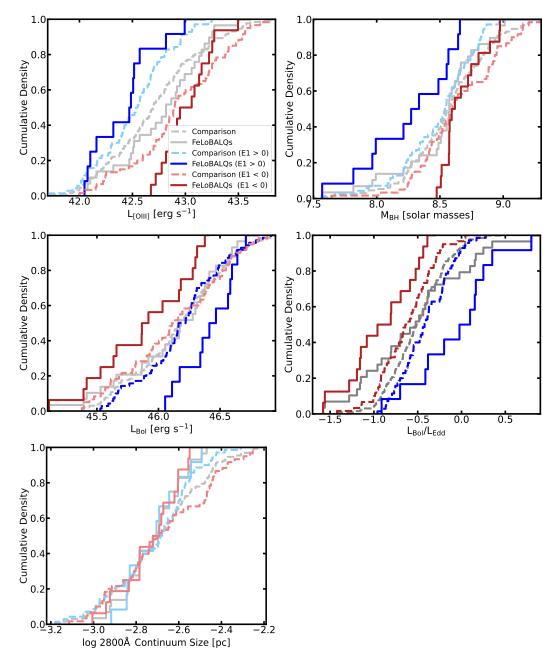


Figure 8. Cumulative distribution plots of the global properties: the integrated [O III] luminosity, the bolometric luminosity, the black hole mass (computed as described in  $\S 2.2$ ), the Eddington ratio  $L_{Bol}/L_{Edd}$ , and the size of the 2800Å continuum emission region. The distributions are consistent between the FeLoBALQs and comparison sample for most of these properties; the exception is the Anderson-Darling detection of a difference in the Eddington ratio. However, the two E1-parameter classes of FeLoBALQs are significantly different for the first four parameters.

reject a unimodal distribution (p = 0.22). We also used the Muratov & Gnedin (2010) GMM method<sup>5</sup> (Muratov & Gnedin 2010). The method fits a two-component gaussian mixture model (GMM) to

 $<sup>^5</sup>$  http://www-personal.umich.edu/ $\sim$ ognedin/gmm/

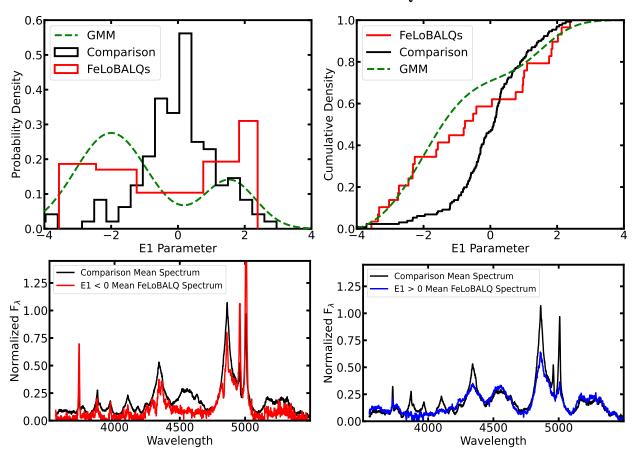


Figure 9. The distribution of the E1 parameter for the FeLoBALQs is different than for the comparison sample. Top: The histogram of the E1 parameter (left) and the cumulative distribution (right). Both plots show that there is an excess of FeLoBALQs at both low and high E1 parameter. The dashed green line shows the two-component Gaussian Mixture Model for the FeLoBAL quasars. Bottom: The weighted mean spectra of the FeLoBALQs with E1 parameter less than zero (left) and greater than zero (right), both compared with the weighted mean spectrum from the comparison sample. The objects with E1 < 0 are characterized by stronger [O III] and weaker Fe II than the mean comparison-sample spectrum, while objects with E1 > 0 are characterized by weaker [O III] and weaker Balmer lines than the mean comparison-sample spectrum.

the data and compares the result to a one-component GMM model using a likelihood ratio. A bootstrap method was used to gauge the robustness of the result. The E1 parameter from the FeLoBAL quasars yielded a probability of p=0.045 that the distribution is unimodal rather than bimodal. The best-fitting two-component GMM<sup>6</sup> is seen as the dashed green line in the top left panel of Fig. 9. The Gaussian parameters were  $\mu_1=1.54$ ,  $\mu_2=-2.0$ ,  $\sigma_1=0.78$ ,  $\sigma_2=1.09$ ,  $N_1=0.42$ ,  $N_2=0.58$ . Note the significant limitation of this method: it assumes that the two distributions are Gaussian, and there is no reason to believe that they should be. Indeed, the cumulative distribution functions shown in the top right panel of Fig. 9 indicate that the two-Gaussian approximation is only an approximate representation of the E1 parameter from the FeLoBAL quasars.

<sup>&</sup>lt;sup>6</sup> https://scikit-learn.org/stable/modules/mixture.html

We divided the samples in two, depending on the sign of the E1 parameter. Note that E1=0 is a representative dividing point because the log [O III] equivalent width and  $R_{\rm FeII}$  were normalized and scaled before E1 was computed. There are 17 (61) and 13 (71) FeLoBALQs (comparison sample objects) with E1 parameter less than and greater than zero, respectively. The weighted mean spectra for these two groups compared with the mean comparison-sample spectrum are shown in the lower panel of Fig. 9. The differences are notable. The FeLoBALQ objects with E1 parameter less than zero are characterized by stronger [O III] and weaker Fe II than the comparison sample average spectrum, while the objects with E1 parameter greater than zero have similar Fe II emission, weaker Balmer lines, and weaker [O III]. It is also notable that the E1 < 0 mean spectrum shows Balmer absorption, seen in the notches in the mean spectrum near 4830 and 4330Å, while the E1 > 0 mean spectrum shows Ca II and He I\* absorption, observed in the scrum of absorption lines near 3900 Å. These different lines point to differences in the physical conditions of the absorbing outflow (Choi et al. 2022). We note that because these are weighted average spectra, they reflect the properties of the objects with the best signal-to-noise spectra.

In §3 we compared the distributions of parameters of the FeLoBALQs with those of the comparison sample. Here we perform the same comparison, but divide the two samples by the E1 parameter. We do this because if the FeLoBALQs are comprised of two classes, then they may differ in different ways from the similarly selected comparison sample; we do see this behavior in the parameter comparison below. We also compare the two groups of FeLoBALQs because significant differences indicate a defining or correlated characteristic property of the two groups.

The cumulative distribution of the E1 parameter is shown in Fig. 10. Blue (red) lines identify the E1 > 0 (E1 < 0) objects, with solid (dashed) lines denoting the FeLoBALQs (comparison) samples. As expected, dividing the data by E1 results in an enormous difference in the E1 parameter distribution.

There are significant difference between the FeLoBAL classes among all of the emission-line properties (Fig. 6). Some of these are expected; for example,  $R_{\text{FeII}}$  and [O III] EW were used to define the E1 parameter. While as a group the [O III] kinematic properties (velocity offset  $v_{50}$  and  $w_{80}$ ) are consistent between the FeLoBALQs and comparison objects, they are significantly different between the E1 < 0 and E1 > 0 FeLoBALQs. The E1 > 0 (E1 < 0) FeLoBALQs are characterized by larger (smaller) velocity offsets and broader (narrower) lines.

The differences between the SPCA coefficients among the different classes is profound. Some dependences are expected because E1 and SPCA coefficient 1 both measure the inverse relationship between the Fe II and [O III] emission. Other dependencies are more subtle. For example, for E1 > 0 FeLoBALQs, SPCA Coefficient 2 is almost never negative. This result means that this eigenvector, characterized by a negative-flux narrow H $\beta$  line, serves to broaden and reduce the flux of the H $\beta$  line in this subclass. It is also interesting that the coefficients of the first eigenvector are sufficient to distinguish between the E1 subgroups of the comparison sample; the remaining three are identical for the E1 subgroups for the comparison sample, but not for the FeLoBALQs. This result demonstrates the tight relationship between the E1 parameter and SPCA1.

The distribution of  $L_{\text{Bol}}$  is seen in (Fig. 8). It is notable that the comparison sample  $L_{\text{Bol}}$  distributions split at E1=0 are consistent, but the FeLoBALQ sample  $L_{\text{Bol}}$  distributions for E1>0 and E1<0 are significantly different (p<0.001; Table 1). The median values for the E1<0 and E1>0 FeLoBALQs are 45.9 and 46.5. The relationship between E1 and  $L_{\text{Bol}}$  is shown in Fig. 11.

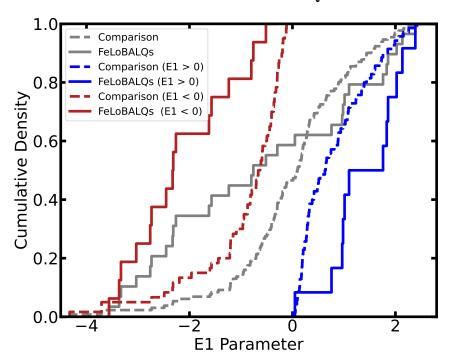


Figure 10. The cumulative distributions of the E1 parameter. The FeLoBAL quasars and comparison sample show dramatically different distributions, both for the whole sample and for the samples divided by positive and negative E1.

Recalling that the FeLoBAL quasars were chosen based solely on their spectroscopic classification, this result seems to be surprising and seems to represent a fundamental property of low redshift FeLoBAL quasars.

The black hole mass in the E1 > 0 FeLoBAL quasars is lower than in the E1 < 0 FeLoBAL quasars, but no such significant difference is present among the comparison objects. Recall that the black hole mass estimate depends on luminosity and the H $\beta$  line width so that more luminous objects with broader lines have larger black-hole masses. In our case, the E1 > 0 (E1 < 0) objects have narrower (broader) H $\beta$  lines and larger (smaller) luminosities so that one might expect that the E1 > 0 and E1 < 0 objects should have more or less the same black hole mass distribution. The differences in luminosity and black hole mass are propagated into  $L_{\rm Bol}/L_{\rm Edd}$ , with the E1 < 0 FeLoBAL quasars accreting at rates more than half a dex lower than the E1 > 0 FeLoBAL quasars. This difference seems to be a fundamental one and an identifying feature of the two groups of FeLoBAL quasars.

Despite the differences in the black hole mass and Eddington ratio distributions, the size of the 2800Å continuum emission region is the same for the E1 < 0 and E1 > 0 objects. The emission region size depends on the temperature distribution as a function of radius. The radius for a particular temperature should be larger for a larger accretion rate, and larger for a larger black hole mass. The black hole mass is larger (smaller) for the E1 < 0 (E1 > 0) objects, but the accretion rate is smaller (larger), so the two effects cancel out.

## 3.4. Spearman-Rank Correlations

The seventeen optical emission line and global properties were correlated against one another for both the FeLoBALQ sample and the comparison sample (Fig. 12). The Spearman Rank correlation

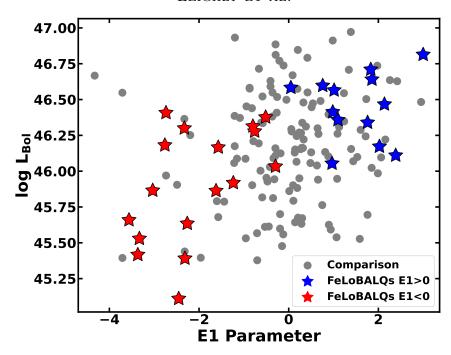


Figure 11. The bolometric luminosity as a function of the E1 parameter. The distribution of the bolometric luminosity for the comparison sample is approximately normal, with no preference for E1 (Fig. 8, while the E1 > 0 (E1 < 0) FeLoBALQs have higher (lower)  $L_{\text{Bol}}$  than average.

is appropriate for these nonparametric data. The plots represent the log of the p value for the correlation, where the sign of the value gives the sense of the correlation. That is, a large negative value implies a highly significant anticorrelation.

Our method for propagating errors was described in §2.2. We chose p < 0.05 as our threshold for significance. The overplotted stars show the fraction of draws that yield p values greater than our threshold value. Generally, taking the errors into account did not affect the significance of a correlation, if present.

As discussed in §3, correlations among quasar properties associated with the Boroson & Green (1992) Eigenvector 1, here parameterized using the E1 parameter, dominate and potentially obscure other correlations. We would like to determine whether there were correlations independent of the E1 parameter. It is also possible that the two classes of FeLoBALQs show different correlation behaviors that would be washed out in the whole-sample correlations. Therefore, we also compute the Spearman-rank correlation coefficient between the parameters divided by E1 < 0 and E1 > 0 (Fig. 12, middle and lower panels).

Some of the correlations we observe are a consequence of parameter dependence. Other correlations are very well known; for example the anticorrelation between  $R_{\text{FeII}}$  and the [O III] equivalent width. The origin of these correlations has been discussed exhaustively in the literature (e.g., Shen & Ho 2014, and references therein). Notable correlations and other patterns in the data are discussed in the sections below.

As discussed in §2.2, the [O III] and Fe II emission is weak in some objects, and it is possible to consider the measurements of those variables that are not found to be significant using the F test to be upper limits. The generalized Kendall Tau test can be used for censored data (Isobe et al. 1986).

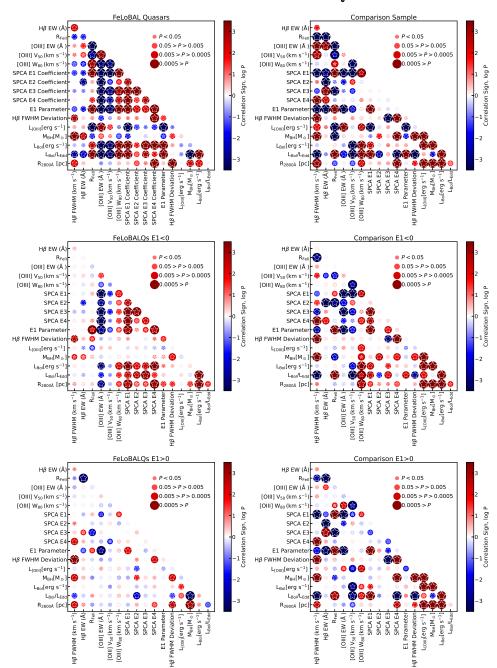


Figure 12. The results of the Spearman rank correlation analysis for the FeLoBAL quasars (left) and the comparison sample (right). The size and color of the marker indicates the sign and p value of the correlation. Anticorelations are shown in blue, and correlations are shown in red. The saturation of the color indicates the significance of the correlation as a continuous variable, while discrete sizes of the points characterizes a range of p values as shown in the legend. The circular markers show the results for parameter values. The stars show the results for a Monte Carlo scheme to estimate the effects of the errors (see text for details). The top panel shows the results for all 30 FeLoBALQs and 132 comparison sample objects, while the two lower panels show the results divided by E1 parameter. Many parameters show similar correlations in both panels; however, some expected correlations, for example between the bolometric luminosity and the [O III] luminosity, are missing in the FeLoBALQ sample.

We use the pymccorrelation implementation (Privon et al. 2020) on the [O III] equivalent width,  $R_{\rm FeII}$  and [O III] luminosity, and looked for parameter combinations that either switched from being a significant correlation (P < 0.05) to insignificant or vice versa. For the FeLoBALQs (including all, E1 > 0, and E1 < 0 combinations), 13 correlations (9% of the 144 non-trivial correlations for these three parameters) changed, with 4 becoming insignificant and 9 becoming significant. For the comparison sample (including all, E1 > 0, and E1 < 0), 12 correlations (8%) changed, with 4 becoming insignificant and 8 becoming significant. We credit these minor changes to the fact that the upper limits only strengthen the observed anticorrelation between [O III] and  $R_{\rm FeII}$  that defined E1 because [O III] (Fe II) was found to statistically unnecessary only among the E1 > 0 (E1 < 0) objects.

## 3.4.1. Shen & Ho 2014

Shen & Ho (2014) presented an analysis of  $\sim 20000$  low-redshift quasars from the SDSS DR7 quasar catalog. They asserted that  $R_{\rm FeII}$  is a measure of the accretion rate relative to the Eddington value (the Eddington ratio), with large values of this parameter corresponding to a large Eddington ratio. They found a wide range of values of H $\beta$  FWHM for a given value of  $R_{\rm FeII}$  and suggested that the dispersion of the H $\beta$  FWHM for a given value of  $R_{\rm FeII}$  reflects a range of viewing angle orientations to a disk-like broad-line region.

We reproduced their Figure 1 for the FeLoBALQs and comparison sample in the left panel of Fig. 13. We already know from §3.2.1 and Fig. 6 that the H $\beta$  FWHM is systematically broader among the FeLoBALQs. This representation shows that the difference is a function of  $R_{\text{FeII}}$  such that objects with larger (smaller) values of  $R_{\text{FeII}}$  have systematically smaller (larger) H $\beta$  FWHM. We highlight the difference by computing the median value in bins of  $R_{\text{FeII}}$  such that each bin has the same number of points: six bins of 22 objects each for the comparison sample and three bins of 10 objects each for the FeLoBALQs.

To quantify the difference, we defined a parameter called H $\beta$  FWHM deviation, abbreviated hereafter as deviation. To compute the deviation for each point, we first linearly interpolate the medians computed above for the comparison sample. For points with larger  $R_{\rm FeII}$  values than the the median of the largest or smallest bin, we used the two nearest median points to extrapolate. The deviation was then defined to be the difference between the log of the observed H $\beta$  FWHM and the log of the interpolated relationship. Shen & Ho (2014) found a lognormal distribution of H $\beta$  FWHM as a function of  $R_{\rm FeII}$  with a dispersion of 0.15–0.25 dex. The disperson in the deviation for the comparison sample is 0.18 and is thus consistent with the Shen & Ho (2014) value.

The cumulative distribution of the deviation is shown in Fig. 13. It is useful to compare this plot with the H $\beta$  FWHM cumulative distribution (Fig. 6). The median values of FWHM for the E1 < 0 and E1 > 0 groups are dramatically different. This result is now explained since the two groups are characterized by much different values of  $R_{\rm FeII}$ , since  $R_{\rm FeII}$  contributes to the definition of the E1 parameter. The deviation parameter takes this difference into account since it is function of  $R_{\rm FeII}$ . The cumulative distributions show that median deviation for the comparison sample is consistent with zero (by definition), and the median value for the FeLoBALQs is 0.17, corresponding to 47% systematically larger H $\beta$  FWHM when averaged over all the objects.

Shen & Ho (2014) conjecture that the deviation in H $\beta$  FWHM at each value of  $R_{\text{FeII}}$  is a consequence of differences in orientation. If true, our result implies the FeLoBALQs are observed at systematically larger inclination angle than objects without absorption. If we take the effective mean inclination

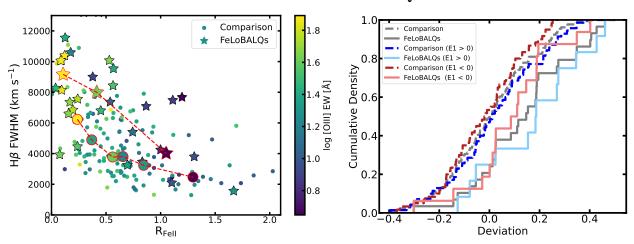


Figure 13. Left: The H $\beta$  FWHM as a function of  $R_{\rm FeII}$  for the FeLoBALQs and comparison sample following Shen & Ho (2014). The large points outlined in red show the median H $\beta$  FWHM values in bins of  $R_{\rm FeII}$ . It is clear that the H $\beta$  FWHM is systematically broader in the FeLoBALQs for a given value of  $R_{\rm FeII}$ . Right: The cumulative distributions of the deviation parameter. The color scheme is the same as used Fig. 6. The deviation parameter separates the FeLoBALQs from the unabsorbed comparison sample more cleanly than does the H $\beta$  FWHM (Fig. 6).

with respect to the normal of unabsorbed objects to be 30 degrees (e.g., Shen & Ho 2014), then assuming the same geometry for the broad-line region and a  $\sin \theta$  dependence, we find that the effective mean inclination to the broad-line quasars should be 48 degrees. The FWHM enters the virial black hole mass as  $FWHM^2$ , so a 47% larger value suggests that the black hole masses for the FeLoBALQs are over-estimated by a factor of 2.2 on average.

A larger inclination viewing angle might be expected for BALQs. Due to the requirement that angular momentum be dispersed for accretion to occur, the accreting gas is expected to be disk-like, not only at the smallest scales (i.e., the optical-UV emitting accretion disk) but also at larger scales (the molecular torus and beyond). If that material is transported perpendicular to the disk by some local mechanism (i.e., radiative line driving, scattering on dust), then once the material rises sufficiently to be illuminated by the brilliant quasar nucleus, the stream lines should be bent radially so that the observer views the quasar nucleus through absorbing gas only along certain lines of sight (e.g., Elvis 2000).

Although promising, a larger inclination viewing angle falls short of explaining all of the differences between the FeLoBALQs and the comparison sample. For example, it does not explain the FeLoBALQ E1 bimodality. Moreover, the explanation is not unique. A broader H $\beta$  emission line would also be produced if the broad-line region were truncated at its outer boundary. Quasars with double-peaked broad lines are extreme examples of such objects (e.g., Strateva et al. 2003), and Fe II absorption has been found in several (Halpern et al. 1996; Halpern 1997; Eracleous et al. 2003). We favor this interpretation and return to this idea in Paper IV (Leighly et al. in prep.).

#### 3.4.2. Boroson 2002

Boroson & Green (1992) presented a principal components analysis of measured emission-line and continuum properties near H $\beta$  in a sample of 87 low-redshift quasars from the Bright Quasar Survey (Hewett et al. 1995). Boroson (2002) used these results augmented by results from a sample of

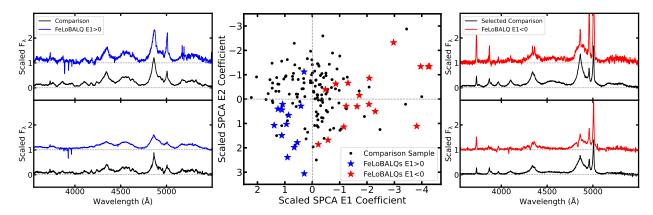


Figure 14. Plots modeled after Fig. 1 and Fig. 2 in Boroson (2002). The central panel shows the spectral PCA fit coefficients scaled by the variance of the comparison sample in each quadrant. The right and left panels show weighted-mean composite spectra from each quadrant offset in the y direction for plot clarity. The highest concentration of FeLoBALQs relative to comparison objects is found in the lower left quadrant, as predicted by Boroson (2002); however, all of the E1 < 0 objects lie in the two right quadrants where Boroson (2002) found radio-loud quasars.

radio-loud objects to investigate the role of the PCA eigenvectors in determining an object's class, i.e., whether an object is radio loud or radio quiet. His sample included a small number of broad absorption line quasars. His discussion culminates in his Fig. 7, an interpretive diagram that used principal components 1 and 2 to classify AGN and quasars.

We present a similar analysis to determine whether the same pattern of behavior is present among our FeLoBALQs and the comparison sample. The difference is that we used the coefficients derived from model fitting using the spectral principal components analysis eigenvectors created from the comparison sample (§2.3). PCA eigenvector coefficients are invariant under sign change, so we use the composite spectra shown in Boroson (2002) Fig. 2 to orient ours. The results are shown in Fig. 14. The negative of our SPCA1 coefficients correspond well with the Boroson (2002) PC1 coefficients. The SPCA2 coefficients correspond less well with the Boroson (2002) PC2 coefficients, so we used the [O III] equivalent width in the composite spectra to assign the negative of our SPCA2 coefficients to the Boroson (2002) PC2 coefficients. Fig. 14 (center) shows the SPCA2 eigenvector coefficients as a function of the SPCA1 eigenvector coefficients. To make the plot more similar to Fig. 1 in Boroson (2002), the SPCA coefficients were scaled by dividing by the the standard deviation of the comparison sample in each quadrant. The FeLoBALQ coefficients are also plotted; their SPCA values have been scaled with the same factors as the comparison sample.

This figure highlights some interesting differences between the comparison objects and the FeLoBAL quasars. There is a striking difference between comparison and FeLoBALQ number density in the left two quadrants. The upper left quadrant includes 30% of the comparison objects, but only one FeLoBALQ, while the lower left quadrant includes 40% of the FeLoBALQs, but only 11% of the comparison objects. Thus there is a strong difference in SPCA2 between the comparison objects and the FeLoBALQs. Examining the composite spectra in the left two panels in Fig. 14 and the PCA eigenvectors in Fig. 4 shows that the difference is that the FeLoBALQs have weaker and broader Balmer emission lines, a property that should correlate with SPCA2. As noted above, a physical interpretation of this result is not obvious.

Boroson (2002) used his Fig. 1 and ensuing discussion to construct a schematic interpretive diagram based on PC1 and PC2 (his Fig. 7). He argued that PC1 is a measure of the Eddington ratio, and PC2 is a measure of the accretion rate which is equivalent to the luminosity for a constant accretion efficiency. Lines of constant black hole mass lie along the diagonal. He found that a plot of PC2 versus PC1 distinguishes between radio-loud and radio-quiet quasars. He concluded that narrow-line Seyfert 1 galaxies and broad absorption line quasars (both generally radio quiet) are characterized by high values of the Eddington ratio, with the BAL quasars additionally characterized by a high accretion rate. Radio-loud objects have larger black hole masses and lower accretion rates.

Comparing the central panel of Fig. 14 with Boroson (2002) Fig. 7 shows that the density of BAL quasars in our sample is high in the lower left quadrant as predicted. A difference is that all of the E1 < 0 FeLoBALQs lie on the right side of the diagram, as they should, since E1 is strongly correlated with the SPCA1 coefficient. The right side of the diagram is where the Boroson (2002) radio-loud objects are. Some of our FeLoBALQs may be radio loud; a systematic investigation of the radio properties of this sample is beyond the scope of this paper. However, we note that SDSS J102226.70+354234.8 has a resolved two-sided jet and E1 = 0.97, and SDSS J164419.75+530750.4 has a 500 kpc scale radio lobe with bilateral hotspots and E1 = -0.51 (L. Morabito, P. Comm., 2021).

Because we have measured the Eddington ratio and can compute the accretion rate, we can directly investigate whether our principal components coefficients correlate with these properties and render the Boroson (2002) Fig. 7 using our measurements (Fig. 15). As shown in Fig. 12, SPCA1 is strongly positively correlated with the Eddington ratio (comparison:  $p = 6.4 \times 10^{-10}$ ; FeLoBALQs:  $p = 3.2 \times 10^{-8}$ ). The accretion rate was computed using  $L_{\rm Bol} = \eta \dot{M} c^2$ , where we assumed a constant  $\eta = 0.1$ , acknowledging that this value may not be accurate at very low or very high accretion rates. The accretion rate is strongly correlated with the SPCA1 coefficients (comparison: p = 0.0022; FeLoBALQ:  $p = 1.1 \times 10^{-6}$ ). It is not strongly correlated with SPCA2 (comparison: p = 0.6; FeLoBALQ: p = 0.014). Thus the x-axis in our figure and the Boroson (2002) Fig. 7 both correspond to the first eigenvector; this is further illustrated by the color bar corresponding to E1 parameter value in Fig. 15. However, our y-axis does not correspond with the second eigenvector. So although we assigned SPCA2 to the y axis in Fig. 14 based on the features in the composite spectra, we did not find that SPCA2 is a measure of the accretion rate, although it does very well separate the E1 > 0 FeLoBALQs from the comparison objects.

In addition, Fig. 15 shows that in our sample the FeLoBAL quasars and comparison sample objects are distributed roughly uniformly in Eddington ratio versus accretion rate space (although statistically distinguishable; see Fig. 9, Fig. 10, Table 2), and are not relegated to high Eddington ratios and high accretion rate, as proposed by Boroson (2002).

We note that other recent work in the UV rest wavelengths does not support the classification scheme proposed by Boroson (2002). There is evidence that the blueshift and equivalent width of the C IV emission line is associated with the Boroson & Green (1992) eigenvector 1 (e.g., Wills et al. 1999; Shang et al. 2003), and therefore by extension the Eddington ratio. Rankine et al. (2020) found that BAL quasars exist throughout C IV blueshift / equivalent width space, and Rankine et al. (2021) showed that radio-loud quasars similarly populate this space. We used Boroson (2002) for our discussion because he used the rest-frame optical eigenvectors and is therefore more similar to our analysis.

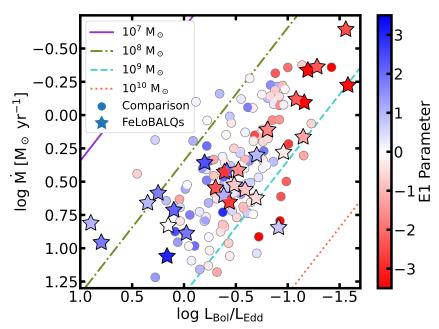


Figure 15. A plot modeled after Fig. 7 in Boroson (2002) rendered using our estimates of the Eddington ratio and accretion rate. Boroson (2002) predicted that BALQs should lie in the lower left corner of this plot, i.e., high Eddington ratio. We found that the FeLoBALQs are characterized by both low and high Eddington ratios, although their distribution in this parameter is statistically different from the distribution of the comparison objects; see Fig. 9, Fig. 10, Table 2.

#### 3.4.3. Correlations Among Global Properties

Next we examined correlations among the global parameters: the black hole mass, bolometric luminosity, and accretion rate relative to Eddington.

We found that the E1 parameter is strongly positively correlated with  $L_{\rm Bol}$  among the FeLoBAL quasars ( $p = 4.4 \times 10^{-5}$ ), but no such correlation is present in the comparison sample (p = 0.15). This result echos Fig. 11, which shows that the E1 < 0 FeLoBALs are less luminous than the E1 > 0 FeLoBALs (§ 3.3). Thus, the optical spectral properties of FeLoBAL quasars in this sample predict the luminosity. This result is surprising and unexpected.

We also investigate the [O III] luminosity. There is a correlation between the bolometric luminosity and the [O III] luminosity in the comparison sample  $(p = 5.2 \times 10^{-19})$ . This type of correlation is expected in a flux-limited sample. The interesting fact is that no correlation is found between these parameters for the FeLoBALQs (p = 0.12). Fig. 16 shows the reason for this behavior. While the correlation in the comparison sample is clearly seen, the FeLoBALQs instead form two (or more) clumps on either side of the comparison sample regression. This behavior further underlines the presence of two types of FeLoBALQs in this sample.

The R<sub>FeII</sub> parameter can be taken as a proxy for the accretion rate relative to Eddington (e.g., Shen & Ho 2014). Fig. 16 shows the relationship between these two parameters. A correlation exists, but it is rough although statistically significant for both the FeLoBALQs and the comparison sample ( $p = 1.2 \times 10^{-4}$  and  $p = 7.1 \times 10^{-11}$ , respectively). Why are these two parameters not perfectly correlated? Several approximations enter into the computation of  $L_{\rm Bol}/L_{\rm Edd}$ .  $L_{\rm Edd}$  depends on the black hole mass. The black hole mass was estimated using the FWHM of the H $\beta$  line and

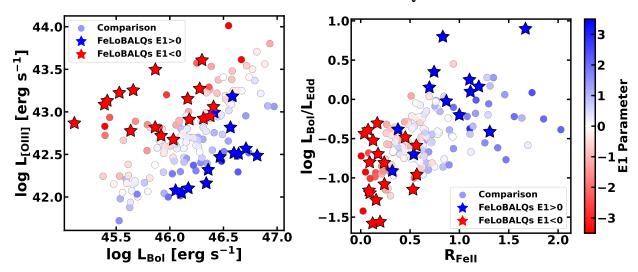


Figure 16. Relationships among global parameters. Left: A strong positive correlation is observed between the bolometric luminosity and the [O III] luminosity for the comparison sample  $(p = 5.2 \times 10^{-19})$ , but not for the FeLoBALQs (p = 0.12). Rather, they form two rough tracks of approximate correlation on either side of the comparison sample objects and divided by E1 parameter. Right: The computed ratio of the bolometric luminosity to the Eddington luminosity as a function of  $R_{FeII}$ . The two parameters are correlated  $(p = 1.2 \times 10^{-4} \text{ for the FeLoBALQs}, \text{ and } p = 7.1 \times 10^{-11} \text{ for the comparison sample})$ .

following the formalism of Collin et al. (2006). In particular, we used their Eq. 7 to estimate the scale factor f based on the FWHM of the H $\beta$  line. This assumption must be a simplification given the systematically broader H $\beta$  lines observed among the FeLoBAL quasars, whether that property originates in a more inclined viewing angle or a lack of a traditional BLR component (or both). If the origin of the broader H $\beta$  lines is viewing angle inclination, then the simplification would bias the black hole masses larger than they should be. Also, we used the measured  $L_{5100}$  luminosity to compute the radius of the broad-line region without correcting for reddening. A too-small  $R_{\rm BLR}$  would bias the black hole mass smaller than they should be.

The bolometric luminosity was computed using a bolometric correction factor from the  $3\mu$ m luminosity density (Gallagher et al. 2007). That bolometric correction factor was computed from relatively luminous quasars which typically show near-infrared emission from a torus. Thus, objects that are weak at three microns will potentially have underestimated bolometric luminosities. In Paper IV, we investigated the optical to IR spectral energy distribution and found that some E1 < 0 objects are weak at 3 microns.

The combination of uncertainties in the black hole mass and bolometric luminosity estimates must contribute to the scatter in  $L_{\rm Bol}/L_{\rm Edd}$  seen in the right panel of Fig. 16. It is interesting that among the E1 < 0 FeLoBALQs,  $L_{\rm Bol}/L_{\rm Edd}$  is correlated with  $L_{\rm Bol}$  but not  $M_{\rm BH}$  ( $p = 5.6 \times 10^-6$  and p = 0.36, respectively), while the opposite is true for the E1 > 0 FeLoBALQs (p = 0.18 and  $p = 1.2 \times 10^{-4}$ , respectively; Fig. 12). It is possible that, in this sample,  $R_{\rm FeII}$  better reflects the physical conditions of the nucleus anticipated to depend on accretion rate than does the computed value of  $L_{\rm Bol}/L_{\rm Edd}$ . It would be interesting to obtain stellar velocity dispersion black hole estimates to substantiate this inference.

A related question is, how interchangable are E1, the first SPCA coefficient,  $R_{\rm FeII}$  and the Eddington ratio? All of these parameters are highly correlated (Fig. 12); the largest p value among all six combinations is  $1.2 \times 10^{-4}$  ( $9.3 \times 10^{-7}$ ) for the FeLoBALs (comparison sample). Yet the E1 parameter is the only one of the four that passes the GMM test for bimodality (§ 3.3), i.e., a distribution with negative kurtosis and a better fit with two heteroskedastic Gaussian distributions than with one, even though bimodality is convincingly established since the distribution fails the non-parametric dip test. At least  $R_{\rm FeII}$  and the Eddington ratio have distributions with negative kurtosis. Perhaps this implies that the E1 parameter captures an essence of the data that is blurred among the other parameters.

# 4. DISCUSSION AND CONCLUSIONS

We presented analysis of the rest-optical spectra near H $\beta$  of a unique sample of low redshift (z < 1) FeLoBAL quasars. All objects have sufficient quality data that the H $\beta$  / [O III] region of the spectrum could be analyzed. Many of the objects were selected using a convolutional neural net (Dabbieri et al. in prep.) applied to 0.8 < z < 1 quasars from the DR14 quasar catalog (Pâris et al. 2018), and of the thirty objects, eleven had not been classified as a BAL quasar previously. A 132-object comparison sample, matched in redshift, median signal-to-noise ratio in the H $\beta$  region, and 3-micron luminosity density was compiled and analyzed in parallel.

BAL quasars can be difficult to find and recognize compared with unabsorbed quasars, and therefore construction of a uniform sample is difficult. The SDSS quasar catalogs require the presence of a broad emission line in the spectrum, and therefore can be biased against heavily absorbed quasars; for example, the spectacular FeLoBAL quasar SDSS J135246.37+423923.5 (Choi et al. 2020) is not in the DR14 quasar catalog. However, our selection process reduces some of the pitfalls of other samples. Although the sample is not large, it is larger than any samples of rest-frame H $\beta$ -region spectra of BAL quasars considered to date (Yuan & Wills 2003; Runnoe et al. 2013; Schulze et al. 2017, 16, 8, 16, respectively). The sample may be more homogeneous, since we chose only FeLoBALQs. BAL quasar properties such as outflow velocity show strong luminosity dependence (e.g., Laor & Brandt 2002; Ganguly et al. 2007). Because our sample spans only a small range of redshift, the range of luminosities is small. The SDSS spectra have more uniform quality than near-infrared spectra can be, due to variable-quality telluric correction and other factors such as fixed pattern noise that degrade the spectra. The ability to compile a large and uniform comparison sample that can be analyzed uniformly turned out to be critical for many of the conclusions in the paper.

Our analysis focused on measurement of the H $\beta$ , [O III], and Fe II. We used traditional multicomponent model fitting, as well as a principal components analysis. We found that the variance in the emission lines in the comparison sample was principally associated with the Boroson & Green (1992) Eigenvector 1, as expected. We defined an empirical parameter E1 which is a function of the [O III] equivalent width and  $R_{\text{FeII}}$ , the ratio of the Fe II emission to the H $\beta$  emission (e.g., Shen & Ho 2014). Both E1 and  $R_{\text{FeII}}$  were found to be strongly correlated with the Eddington ratio (Fig. 12, 16). A large and positive E1 parameter corresponds to a high Eddington ratio, while a large an negative E1 parameter corresponds to a low Eddington ratio.

The large and well-defined matched sample of unabsorbed quasars allowed us to test whether low-redshift FeLoBAL quasars have the same rest-frame optical emission line properties as unabsorbed objects. The principal result of the paper is that they do not. The uanbsorbed quasars have a peaked distribution in the E1 parameter (Fig. 9). In contrast, the FeLOBALQs show an apparent

bimodal distribution in E1, although not statistically significant. Moreover, the luminosities of the two groups of FeLOBALQs is different (Fig. 8, Fig. 11), and those differences carry over to a difference in Eddington ratio (Fig. 8). The implication is that the low-redshift FeLoBALQs are characterized by either a large Eddington ratio, or a small one, but not an intermediate value. This division is echoed in the relationship between the [O III] and  $L_{\rm Bol}$ . These parameters are correlated in the comparison sample, but clustered by E1 in the FeLoBAL quasars (§3.4.3; Fig. 16).

This result is new and distinct from what has been previously reported in the literature. Less work has been done in the rest-frame optical band compared with the rest-frame UV; nevertheless, it has been reported that BAL quasars appear to be either high Eddington ratio objects (Yuan & Wills 2003; Runnoe et al. 2013), or that there is no difference between absorbed and unabsorbed objects (Schulze et al. 2017). The difference between our results and the previous ones likely stems from the large and uniform parent sample: the low redshift SDSS quasar catalog, supplemented by FeLoNET, our convolutional neural net, used to discover more than half of the FeLoBALQs analyzed here. This result inspires the question: why does FeLoBAL absorption occur in objects with high and low accretion rates, but not in objects with an intermediate accretion rate? This question is addressed in Paper IV (Leighly et al. in prep.).

We found that the measurements of H $\beta$  FWHM of the FeLoBALQs are consistently larger than those of the comparison sample (Fig. 6). Moreover, they are consistently larger for the same value of  $R_{\text{FeII}}$  (§3.4.1, Fig. 13). Shen & Ho (2014) proposed that  $R_{\text{FeII}}$  corresponds to Eddington ratio, and that the scatter in H $\beta$  width indicates objects with different inclination angles. If this interpretation is correct for the FeLoBAL quasars, then if normal quasars are typically observed at 30 degrees from normal to the accretion disk, the FeLoBALQs are typically observed at 48 degrees. However, this reasoning does not explain all of the many differences we found between the FeLoBAL quasars and the unabsorbed comparison sample; for example, it does not explain the apparent bimodality in the FeLoBAL distribution. Moreover, this explanation is not unique. Instead, the narrow core of the H $\beta$  emission line may be missing. Additional support for this idea is presented and discussed in Paper IV (Leighly et al. in prep.).

We compared our results with those of Boroson (2002). He found evidence that the rest-frame optical band PCA eigenvector coefficients could be used to separate quasars among narrow-line Seyfert 1 galaxies, BAL quasars and radio-loud objects. In particular, he found that BAL quasars were relegated to a corner of the PCA1-PCA2 coefficient graph. We confirmed that nearly all of our E1 > 0 (high Eddington ratio) FeLoBAL quasars fell in that region of parameter space. However, we found that all of our E1 < 0 were scattered among the radio-loud objects in the Boroson (2002) scheme. We are in the process of investigating the radio properties of this sample. We also note that more recent work using rest-frame UV spectra has found a more uniform distribution of types of objects (e.g., Rankine et al. 2020, 2021).

Moving forward, we note that the Fe II absorption spectrum blankets the rest-frame UV region and FeLoBAL quasars can be observed to resdshifts higher than  $z \sim 3$ . In a flux-limited sample like the SDSS, higher redshift samples are comprised of higher luminosity objects. Assuming fixed Eddington ratio distribution, such objects will have larger black hole masses. A larger black hole mass will have a softer (UV dominant) spectral energy distribution, which could affect the outflow in two ways. The softer SED might produce an outflow with a different ionization balance, i.e., a larger fraction of lower-ionization species, which means the observed absorption could change. A dramatic change

is probably not expected; the observed absorption lines should depend principally on the ionization parameter, as is usually the case. The softer SED should be more efficient in accelerating outflows, since it has more photons with wavelengths suitable for resonance scattering and fewer likely to overionize the outflowing gas. In fact, we see some evidence for faster outflows and shifted parameters among the higher redshift FeLoBAL quasars we have analyzed already (Voelker et al. 2021). We also expect that lower-Eddington-ratio objects will be rarer (e.g., Jester et al. 2005). This is because the black hole mass function is steep and objects with black holes larger than  $10^{10} \,\mathrm{M}_{\odot}$  are very rare.

#### ACKNOWLEDGMENTS

KML acknowledges very useful conversations with Leah Morabito, and thanks Alex Parsells for running the Hartigan & Hartigan (1985) dip test. Support for SimBAL development and analysis is provided by NSF Astronomy and Astrophysics Grants No. 1518382 and 2006771. This work was performed in part at Aspen Center for Physics, which is supported by National Science Foundation grant PHY-1607611. SCG thanks the Natural Science and Engineering Research Council of Canada.

Long before the University of Oklahoma was established, the land on which the University now resides was the traditional home of the "Hasinais" Caddo Nation and "Kirikiris" Wichita & Affiliated Tribes. This land was also once part of the Muscogee Creek and Seminole nations.

We acknowledge this territory once also served as a hunting ground, trade exchange point, and migration route for the Apache, Comanche, Kiowa and Osage nations. Today, 39 federally-recognized Tribal nations dwell in what is now the State of Oklahoma as a result of settler colonial policies designed to assimilate Indigenous peoples.

The University of Oklahoma recognizes the historical connection our university has with its Indigenous community. We acknowledge, honor and respect the diverse Indigenous peoples connected to this land. We fully recognize, support and advocate for the sovereign rights of all of Oklahoma's 39 tribal nations.

This acknowledgement is aligned with our university's core value of creating a diverse and inclusive community. It is our institutional responsibility to recognize and acknowledge the people, culture and history that make up our entire OU Community.

Funding for the SDSS and SDSS-II has been provided by the Alfred P. Sloan Foundation, the Participating Institutions, the National Science Foundation, the U.S. Department of Energy, the National Aeronautics and Space Administration, the Japanese Monbukagakusho, the Max Planck Society, and the Higher Education Funding Council for England. The SDSS Web Site is http://www.sdss.org/.

The SDSS is managed by the Astrophysical Research Consortium for the Participating Institutions. The Participating Institutions are the American Museum of Natural History, Astrophysical Institute Potsdam, University of Basel, University of Cambridge, Case Western Reserve University, University of Chicago, Drexel University, Fermilab, the Institute for Advanced Study, the Japan Participation Group, Johns Hopkins University, the Joint Institute for Nuclear Astrophysics, the Kavli Institute for Particle Astrophysics and Cosmology, the Korean Scientist Group, the Chinese Academy of Sciences (LAMOST), Los Alamos National Laboratory, the Max-Planck-Institute for Astronomy (MPIA), the Max-Planck-Institute for Astrophysics (MPA), New Mexico State University, Ohio State University, University of Pittsburgh, University of Portsmouth, Princeton University, the United States Naval Observatory, and the University of Washington.

Funding for SDSS-III has been provided by the Alfred P. Sloan Foundation, the Participating Institutions, the National Science Foundation, and the U.S. Department of Energy Office of Science. The SDSS-III web site is http://www.sdss3.org/.

SDSS-III is managed by the Astrophysical Research Consortium for the Participating Institutions of the SDSS-III Collaboration including the University of Arizona, the Brazilian Participation Group, Brookhaven National Laboratory, Carnegie Mellon University, University of Florida, the French Participation Group, the German Participation Group, Harvard University, the Institute de Astrofisica de Canarias, the Michigan State/Notre Dame/JINA Participation Group, Johns Hopkins University, Lawrence Berkeley National Laboratory, Max Planck Institute for Astrophysics, Max Planck Institute for Extraterrestrial Physics, New Mexico State University, New York University, Ohio State University, Pennsylvania State University, University of Portsmouth, Princeton University, University of Virginia, University of Washington, and Yale University.

Facility: IRTF (SpeX)

Software: emcee (Foreman-Mackey et al. 2013), Cloudy (Ferland et al. 2013), pymccorrelation (Privon et al. 2020), mlinmix\_err (Kelly 2007), Sherpa (Freeman et al. 2001), SimBAL (Leighly et al. 2018), GMM (Muratov & Gnedin 2010)

## REFERENCES

Akritas, M. G., & Bershady, M. A. 1996, ApJ, 470, 706

Bailey, S. 2012, PASP, 124, 1015

Baldwin, J. A. 1977, ApJ, 214, 679

Baskin, A., Laor, A., & Hamann, F. 2015, MNRAS, 449, 1593

Bentz, M. C., Peterson, B. M., Pogge, R. W., Vestergaard, M., & Onken, C. A. 2006, ApJ, 644, 133

Bevington, P. R. 1969, Data reduction and error analysis for the physical sciences

Boroson, T. A. 2002, ApJ, 565, 78

Boroson, T. A., & Green, R. F. 1992, ApJS, 80, 109

Brotherton, M. S., Wills, B. J., Francis, P. J., & Steidel, C. C. 1994, ApJ, 430, 495

Choi, H., Leighly, K. M., Terndrup, D. M., et al. 2022, arXiv e-prints, arXiv:2203.11964

Choi, H., Leighly, K. M., Terndrup, D. M., Gallagher, S. C., & Richards, G. T. 2020, ApJ, 891, 53

Coatman, L., Hewett, P. C., Banerji, M., et al. 2017, MNRAS, 465, 2120

Cohen, R. D. 1983, ApJ, 273, 489

Collin, S., Kawaguchi, T., Peterson, B. M., & Vestergaard, M. 2006, A&A, 456, 75 Corbin, M. R., & Boroson, T. A. 1996, ApJS, 107, 69

Dabbieri, C., Leighly, K., & Richards, G. 2020, in American Astronomical Society Meeting Abstracts, Vol. 236, American Astronomical Society Meeting Abstracts #236, 238.03

de Kool, M., Arav, N., Becker, R. H., et al. 2001, ApJ, 548, 609

de Kool, M., Becker, R. H., Gregg, M. D., White, R. L., & Aray, N. 2002, ApJ, 567, 58

Elvis, M. 2000, ApJ, 545, 63

Eracleous, M., Halpern, J. P., & Charlton, J. C. 2003, ApJ, 582, 633

Ferland, G. J., Porter, R. L., van Hoof, P. A. M., et al. 2013, RMxAA, 49, 137

Foreman-Mackey, D., Hogg, D. W., Lang, D., & Goodman, J. 2013, PASP, 125, 306

Francis, P. J., Hewett, P. C., Foltz, C. B., & Chaffee, F. H. 1992, ApJ, 398, 476

Frank, J., King, A., & Raine, D. J. 2002, Accretion Power in Astrophysics: Third Edition

- Freeman, P., Doe, S., & Siemiginowska, A. 2001, in Society of Photo-Optical Instrumentation
  Engineers (SPIE) Conference Series, Vol. 4477,
  Society of Photo-Optical Instrumentation
  Engineers (SPIE) Conference Series, ed. J.-L.
  Starck & F. D. Murtagh, 76–87
- Gallagher, S. C., Richards, G. T., Lacy, M., et al. 2007, ApJ, 661, 30
- Ganguly, R., Brotherton, M. S., Cales, S., et al. 2007, ApJ, 665, 990
- Gibson, R. R., Jiang, L., Brandt, W. N., et al. 2009, ApJ, 692, 758
- Giustini, M., & Proga, D. 2019, A&A, 630, A94 Grupe, D. 2004, AJ, 127, 1799
- Hall, P. B., Anderson, S. F., Strauss, M. A., et al. 2002, ApJS, 141, 267
- Halpern, J. P. 1997, in Astronomical Society of the Pacific Conference Series, Vol. 128, Mass Ejection from Active Galactic Nuclei, ed.
  N. Arav, I. Shlosman, & R. J. Weymann, 41
- Halpern, J. P., Eracleous, M., Filippenko, A. V.,& Chen, K. 1996, ApJ, 464, 704
- Hamann, F., Herbst, H., Paris, I., & Capellupo,D. 2019, MNRAS, 483, 1808
- Hartigan, J. A., & Hartigan, P. M. 1985, The Annals of Statistics, 13, 70
- Hewett, P. C., & Foltz, C. B. 2003, AJ, 125, 1784Hewett, P. C., Foltz, C. B., & Chaffee, F. H. 1995, AJ, 109, 1498
- Isobe, T., Feigelson, E. D., Akritas, M. G., & Babu, G. J. 1990, ApJ, 364, 104
- Isobe, T., Feigelson, E. D., & Nelson, P. I. 1986, ApJ, 306, 490
- Jester, S., Schneider, D. P., Richards, G. T., et al. 2005, AJ, 130, 873
- Kelly, B. C. 2007, ApJ, 665, 1489
- Knigge, C., Scaringi, S., Goad, M. R., & Cottis, C. E. 2008, MNRAS, 386, 1426
- Kovačević, J., Popović, L. Č., & Dimitrijević, M. S. 2010, ApJS, 189, 15
- Krawczyk, C. M., Richards, G. T., Gallagher,S. C., et al. 2015, AJ, 149, 203
- Laor, A., & Brandt, W. N. 2002, ApJ, 569, 641Leighly, K. M. 2004, ApJ, 611, 125
- Leighly, K. M., Terndrup, D. M., Gallagher, S. C., Richards, G. T., & Dietrich, M. 2018, ApJ, 866, 7
- Leighly, K. M., Terndrup, D. M., Lucy, A. B., et al. 2019, ApJ, 879, 27

- Ludwig, R. R., Wills, B., Greene, J. E., & Robinson, E. L. 2009, ApJ, 706, 995
- Muratov, A. L., & Gnedin, O. Y. 2010, ApJ, 718, 1266
- Pâris, I., Petitjean, P., Rollinde, E., et al. 2011, A&A, 530, A50
- Pâris, I., Petitjean, P., Ross, N. P., et al. 2017, A&A, 597, A79
- Pâris, I., Petitjean, P., Aubourg, É., et al. 2018, A&A, 613, A51
- Privon, G. C., Ricci, C., Aalto, S., et al. 2020, ApJ, 893, 149
- Rankine, A. L., Hewett, P. C., Banerji, M., & Richards, G. T. 2020, MNRAS, 492, 4553
- Rankine, A. L., Matthews, J. H., Hewett, P. C., et al. 2021, MNRAS, 502, 4154
- Reichard, T. A., Richards, G. T., Hall, P. B., et al. 2003, AJ, 126, 2594
- Runnoe, J. C., Ganguly, R., Brotherton, M. S., & DiPompeo, M. A. 2013, MNRAS, 433, 1778
- Sawicki, M. 2012, PASP, 124, 1208
- Schulze, A., Schramm, M., Zuo, W., et al. 2017, ApJ, 848, 104
- Shang, Z., Wills, B. J., Robinson, E. L., et al. 2003, ApJ, 586, 52
- Shen, Y. 2016, ApJ, 817, 55
- Shen, Y., & Ho, L. C. 2014, Nature, 513, 210
- Strateva, I. V., Strauss, M. A., Hao, L., et al. 2003, AJ, 126, 1720
- Sulentic, J. W., Marziani, P., & Dultzin-Hacyan, D. 2000, ARA&A, 38, 521
- Tolea, A., Krolik, J. H., & Tsvetanov, Z. 2002, ApJL, 578, L31
- Trump, J. R., Hall, P. B., Reichard, T. A., et al. 2006, ApJS, 165, 1
- Véron-Cetty, M.-P., Joly, M., & Véron, P. 2004, A&A, 417, 515
- Voelker, J., Choi, H., Leighly, K., DeFrancesco, C.,
  & Dabbieri, C. 2021, in American Astronomical
  Society Meeting Abstracts, Vol. 53, American
  Astronomical Society Meeting Abstracts, 337.10
- Wang, J., Wei, J. Y., & He, X. T. 2006, ApJ, 638, 106
- Weymann, R. J., Morris, S. L., Foltz, C. B., & Hewett, P. C. 1991, ApJ, 373, 23
- Wills, B. J., Laor, A., Brotherton, M. S., et al. 1999, ApJL, 515, L53
- Wolf, J., Salvato, M., Coffey, D., et al. 2020, MNRAS, 492, 3580

Yi, W., Brandt, W. N., Hall, P. B., et al. 2019, ApJS, 242, 28

Yip, C. W., Connolly, A. J., Vanden Berk, D. E., et al. 2004, AJ, 128, 2603

Yuan, M. J., & Wills, B. J. 2003, ApJL, 593, L11 Zakamska, N. L., & Greene, J. E. 2014, MNRAS, 442, 784